Old Dominion University

ODU Digital Commons

2021

Pore Water Exchange-Driven Inorganic Carbon Export From Intertidal Salt Marshes

Joeseph J. Tamborski
Old Dominion University, jtambors@odu.edu

Meagan Eagle

Barret L. Kurylyk

Kevin D. Kroeger

Zhaoihui Aleck Wang

See next page for additional authors

Authors

Joeseph J. Tamborski, Meagan Eagle, Barret L. Kurylyk, Kevin D. Kroeger, Zhaoihui Aleck Wang, Paul Henderson, and Matthew A. Charette

Pore water exchange-driven inorganic carbon export from intertidal salt marshes

Joseph J. Tamborski [1,2,3]*, Meagan Eagle,[4] Barret L. Kurylyk,[2] Kevin D. Kroeger,[4] Zhaoihui Aleck Wang,[1] Paul Henderson,[1] Matthew A. Charette[1]

[1]Department of Marine Chemistry and Geochemistry, Woods Hole Oceanographic Institution, Woods Hole, Massachusetts
[2]Centre for Water Resources Studies and Department of Civil and Resource Engineering, Dalhousie University, Halifax, Nova Scotia, Canada
[3]Department of Ocean and Earth Sciences, Old Dominion University, Norfolk, Virginia
[4]U.S. Geological Survey, Woods Hole Coastal and Marine Science Center, Woods Hole, Massachusetts

Abstract

Respiration in intertidal salt marshes generates dissolved inorganic carbon (DIC) that is exported to the coastal ocean by tidal exchange with the marsh platform. Understanding the link between physical drivers of water exchange and chemical flux is a key to constraining coastal wetland contributions to regional carbon budgets. The spatial and temporal (seasonal, annual) variability of marsh pore water exchange and DIC export was assessed from a microtidal salt marsh (Sage Lot Pond, Massachusetts). Spatial variability was constrained from $^{224}Ra : ^{228}Th$ disequilibria across two hydrologic units within the marsh sediments. Disequilibrium between the more soluble ^{224}Ra and its sediment-bound parent ^{228}Th reveals significant pore water exchange in the upper 5 cm of the marsh surface (0–36 L m^{-2} d^{-1}) that is most intense in low marsh elevation zones, driven by tidal overtopping. Surficial sediment DIC transport ranges from 0.0 to 0.7 g C m^{-2} d^{-1}. The sub-surface sediment horizon intersected by mean low tide was disproportionately impacted by tidal pumping (20–80 L m^{-2} d^{-1}) and supplied a seasonal DIC flux of 1.7–5.4 g C m^{-2} d^{-1}. Export exceeded 10 g C m^{-2} d^{-1} for another marsh unit, demonstrating that fluxes can vary substantially across salt marshes under similar conditions within the same estuary. Seasonal and annual variability in marsh pore water exchange, constrained from tidal time-series of radium isotopes, was driven in part by variability in mean sea level. Rising sea levels will further inundate high marsh elevation zones, which may lead to greater DIC export.

Tidal wetlands play an intricate role in the coastal carbon cycle (Herrmann et al. 2015; Najjar et al. 2018). Per unit area, salt marshes store significantly more carbon (i.e., "blue carbon") than terrestrial ecosystems (Mcleod et al. 2011; Bauer et al. 2013). Carbon generated in salt marshes is preserved through burial, transformed internally via microbial decomposition of organic matter and exported laterally via tidal pumping (Wang and Cai 2004; Cai 2011). Carbon outwelling exceeds tidal wetland carbon burial by a factor of five along eastern North America, with approximately equal contributions from dissolved organic carbon and dissolved inorganic carbon (DIC) species (Najjar et al. 2018). However, DIC flux estimates are based on limited study sites, resulting in large uncertainties in coastal carbon budgets (Neubauer and Anderson 2003; Wang and Cai 2004; Wang et al. 2016). Spatial and temporal variability in DIC export is poorly understood (Chu et al. 2018), thus resolving flux variability is necessary to improve regional carbon budgets and forecast changes in the coastal carbon cycle.

Carbon outwelling is intimately linked to marsh hydrogeology (Santos et al. 2019); thus, external drivers of marsh hydrogeology should be well characterized to estimate carbon flux (Guimond et al. 2020b). Marsh soil composition is generally composed of a mixture of sand, silt, clay, and organic matter, with macropore structures that generate hydraulic conductivities comparable to that of fine sands (Harvey and Nuttle 1995). Intertidal salt marsh zonation is largely controlled by surface elevation and tidal flooding, forming distinct low marsh and high marsh elevation and vegetation zones. The terrestrial groundwater table and sea-level interact with the marsh surface elevation gradient to drive variability in subsurface flow (Guimond et al. 2020b), with notable differences between shallow (surficial) and deep flow paths across the marsh

*Correspondence: jtambors@odu.edu

Additional Supporting Information may be found in the online version of this article.

platform. Shallow flow paths are influenced by topographic and tidal gradients (Harvey et al. 1987; Nuttle and Hemmond 1988; Xin et al. 2011), macro-pore structures (Harvey and Nuttle 1995), bioirrigation and bioturbation (Guimond et al. 2020a; Xiao et al. 2019), evapotranspiration (Xin et al. 2013), vegetation type, and depth of the active root zone (Moffett et al. 2012). Deep flow paths will vary with spatial position across the marsh (creek bank vs. marsh interior) (Wilson and Gardner 2006; Wilson and Morris 2012). Rising tides laterally recharge the creek bank (Xin et al. 2011), such that creek bank hydrogeology is generally distinct from that of the marsh interior (Moffett et al. 2012). Variability in water exchange between different marsh zones thus impacts the inventory of pore water DIC available for exchange, through both the delivery of new oxidants to the subsurface and variation in residence time.

Naturally occurring radium isotopes have a proven utility as tracers of salt marsh hydrogeology and solute export (Bollinger and Moore 1993; Rama and Moore 1996; Krest et al. 2000). The Ra quartet has a wide range of half-lives (^{223}Ra = 11.4 d, ^{224}Ra = 3.7 d, ^{226}Ra = 1600 y, ^{228}Ra = 5.75 y) that enable tracing subsurface flow paths over different spatial and temporal scales. Recent analytical advances have allowed the measurement of surface-exchangeable ^{224}Ra and its sediment-bound parent ^{228}Th ($t_{1/2}$ = 1.9 y) from sediment core measurements (Cai et al. 2012). Deficits of ^{224}Ra with respect to ^{228}Th in sediment profiles are produced by the recent (~ 1–10 d) transport of the more soluble ^{224}Ra daughter. The ^{224}Ra : ^{228}Th disequilibria technique can be used to determine the transfer of dissolved solutes, including DIC (Cai et al. 2015), across the marsh sediment–water interface. In layered marsh systems, application of the ^{224}Ra : ^{228}Th disequilibria technique can be used to quantify lateral water and solute fluxes at depth (Shi et al. 2019). The ^{224}Ra : ^{228}Th technique may therefore be a valuable tool to characterize key depth horizons of DIC export from intertidal salt marshes.

The aim of the present study is to constrain the magnitude and spatial extent of pore water exchange-driven DIC export from intertidal salt marshes. Identifying the principal spatial zones of carbon export and flux variability within the marsh over time is key to improving coastal carbon budgets (Najjar et al. 2018). At this site, and many other coastal wetlands, lateral carbon export includes both marsh pore water exchange and submarine groundwater discharge derived DIC. An additional, outstanding question concerns the relative importance of terrestrial submarine groundwater discharge in supplying a new, external source of DIC, as compared to marsh pore water exchange. Herein we constrain the spatial variability in marsh pore water exchange and DIC flux (distance from tidal creek and relative depth zones) from ^{224}Ra : ^{228}Th sediment core analyses (Shi et al. 2019). In addition, we present tidal creek time-series data, which provide a near instantaneous flux estimate, to evaluate seasonal and inter-annual variability in marsh pore water exchange and submarine groundwater discharge, constrained from Ra isotope end-member mixing models (Charette 2007). We follow the terminology outlined by Harvey and Odum (1990), where *groundwater discharge* is defined as groundwater originating from the underlying sand aquifer and *pore water exchange* is the exchange of interstitial waters (infiltration of seawater or precipitation) draining from the marsh peat. Note that marsh pore water exchange is not bound by the spatial and temporal scales defined by Taniguchi et al. (2019).

Material and methods

Study site

Sage Lot Pond (Fig. 1), located along the southern coast of Cape Cod, Massachusetts, is a fringing marsh system with a mean semi-diurnal tidal range of 0.4 m. The relative rate of sea-level rise in this region is 2.92 ± 0.17 mm y^{-1} (NOAA station 8447930, Woods Hole, Massachusetts). Crab burrow density is relatively low and increases with increasing unvegetated area (station "WQB"; $<< 50$ burrows m^{-2}; Wasson et al. 2019). We studied two separate hydrologic units within Sage Lot Pond to assess spatial variability in marsh pore water exchange and DIC flux. Marsh site 1 has a drainage basin of 4132 m^2 (Wang et al. 2016) and is hypothesized to be impacted by a relatively small volume of fresh groundwater discharge, estimated as 5.4×10^4 m^3 y^{-1}, or $\sim 3\%$ of the mean annual tidal flow (Wang et al. 2016; Chu et al. 2018). Low marsh areas are dominated by *Spartina alterniflora*, with an average peat thickness of 150 cm and dry bulk density of ~ 0.1–0.2 g cm^{-3}. In comparison, marsh site 2 (3306 m^2) is characterized by a greater abundance of low marsh area and panne/pools (Fig. 1D). The average peat thickness of marsh site 2 (70 cm) is half that of marsh site 1. No prior information exists on the hydrogeology of marsh site 2.

Field methods

Sampling campaigns were carried out between 2015 and 2019 at Sage Lot Pond. Tidal time-series measurements were conducted during winter 2018 (December), spring 2015 and 2016 (April), summer 2015, 2016, and 2019 (June and July), and fall 2015, 2016 and 2019 (October and November) at the mouth of the tidal creek at marsh site 1. A multiparameter sonde (YSI) and acoustic doppler current profiler were stationed at the mouth of the tidal creek, with 10-min data recording intervals continuously in 2015 and 2016 and over a several week period in 2018 and 2019 (Fig. 1C). Multiparameter sensors included conductivity and salinity, temperature, water depth, dissolved oxygen and pH. All sensors were calibrated and cleaned prior to each field deployment. The dissolved oxygen sensor failed during the winter 2018 deployment, and the pH sensor failed during the June 2019 deployment. Creek waters were collected every 60–80 min for dissolved Ra isotopes (~ 20–40 L) over discrete 12-h tidal cycles from a submersible well pump deployed ~ 30 cm from the creek bottom. In parallel, tidal creek waters for DIC
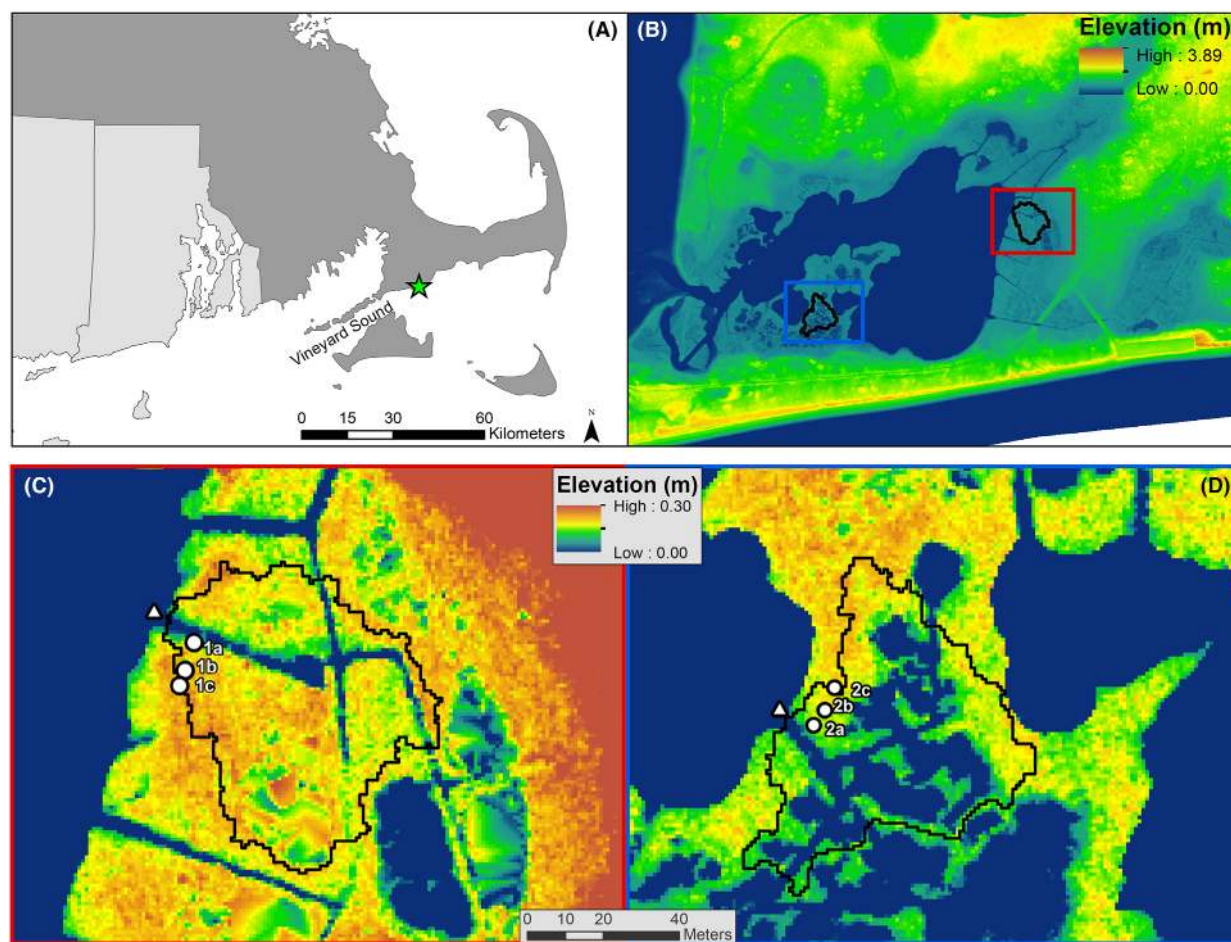
Fig. 1. Sage Lot Pond, located within the Waquoit Bay National Estuarine Research Reserve (WBNERR), Massachusetts (**A**,**B**). Pore water and sediment core sampling stations for marsh site 1 (red box; (**C**) and marsh site 2 (blue box; **D**) are depicted by white circles (a = creek; b = mid; c = interior). The tidal creek mouth sampling location is depicted by a white triangle in panel (**C**). The solid black lines represent the marsh drainage basins, and lidar elevation is indicated by color.

determination were filtered through 0.45-μm capsule filters into 250-mL borosilicate glass bottles following Wang et al. (2016) for winter, summer and fall 2019 campaigns. Tidal time-series data from 2015 and 2016 are publicly available, including tidal creek Ra and DIC concentrations (Mann et al. 2019; Brooks et al. 2021) and were used to estimate DIC flux in Chu et al. (2018).

Sediment cores and pore waters were sampled from two marsh hydrologic units (sites) during 2018 and 2019, with stations designated as creek, mid, and interior. These stations were approximately 1.5, 7.5, and 14 m away from the creek bank for marsh sites 1 and 2 (Fig. 1). Elevation at each station was measured with a Trimble RTK-GPS system, with an elevation accuracy of 2–3 cm, relative to the North American Vertical Datum of 1988 (NAVD88). All stations were sampled for sediment cores and pore water profiles during winter 2018 (0–25 cm depths) and summer 2019 (site 1 = 0–150 cm; site 2 = 0–80 cm; both to the peat-sand interface). Marsh site 1

creek and mid stations were additionally sampled during April 2019 (0–10 cm) and November 2019 (0–150 cm). All stations were sampled during moderately calm field conditions except for the mid station at marsh site 2 during summer 2019, which was sampled the day following a moderate precipitation event (35.4 mm, 23 July 2019).

Sediment cores for ^{224}Ra : ^{228}Th analyses were collected around low tide for all sampling dates. To prevent sediment compaction, cores were collected using a stainless-steel Russian Peat Borer (AMS, Inc.). This device cuts the core longitudinally, resulting in a semicylindrical core. Thus, multiple cores were collected from the same location to retrieve enough mineral mass for radionuclide analyses. Cores were immediately sectioned in the field into 1-cm (0–5 cm depth), 2-cm (5–50 cm depth) or 3-cm (50–150-cm depth) thick slices and placed into individual containers for later processing.

Shallow pore waters (1 and 5 cm) were hand collected from push-point sippers via syringe and filtered (0.45 μm) with

sample volumes of 50–100 mL for Ra analyses and 1–3 mL for DIC analyses; these shallow samples integrate over a maximum depth of ~ 2 cm assuming equal horizontal and vertical hydraulic conductivity. Deeper pore waters were sampled from a steel-tip push-point piezometer (MHE products) and retrieved using a peristaltic pump at a flow rate of < 0.1 L min^{-1}; these deep samples integrate over a maximum depth of ~ 6 cm. Groundwater samples from the sandy aquifer unit beneath the marsh peat ($\sim 145–175$ cm) were collected during summer and fall 2019. Deep pore water (≥ 10 cm) and groundwater Ra isotope samples ($\sim 0.25–4$ L) were collected from discrete depths (seasonally variable) and field-filtered with 0.45-μm capsule filters. DIC samples were collected from all depths; samples (3 mL) were collected without bubbles into syringes, filtered on-site (0.20 μm), injected into helium flushed 5-mL vials and immediately stored on ice.

Water samples

Pore water and groundwater DIC concentrations were analyzed using a CO_2 coulometer (Dickson et al. 2007). Samples were acidified with 20% H_3PO_4 to convert all inorganic carbon species to CO_2, stripped with a helium carrier gas, adsorbed by an ethanolamine solution and titrated using thymolphalein as an indicator. Certified reference materials for seawater DIC (obtained from A. Dickson from the Scripps Institute of Oceanography) were run at the beginning and end of each analysis period, and after every 4–5 samples, to calibrate the coulometer system. Measurement uncertainty is ~ 1–2%, based on replicate reference material runs. Tidal creek DIC samples were analyzed on a LiCOR Apollo system with an analytical precision of ± 2.0 μmol kg^{-1}, following the methods outlined in Wang et al. (2016).

For radium analysis, water samples were slowly filtered (< 0.5 L min^{-1}) through MnO$_2$-coated acrylic fibers, rinsed with Ra-free Milli-Q water and partially dried. Anoxic pore waters were oxidized by adding ~ 100 mL of sodium hypochlorite to prevent the reduction of Mn bound to the acrylic fiber. Samples were counted on a RaDeCC system to determine the initial ^{224}Ra activity and ~ 25 d after collection to determine the ^{224}Ra activity supported by ^{228}Th (Moore and Arnold 1996). ^{223}Ra is not discussed in this study. Upon completion, fibers were either ashed (tidal creek samples; 820°C for 12 h) or dried (select pore water samples; 40°C for 24 h), homogenized and placed in polystyrene counting vials and sealed with epoxy for > 3 weeks to allow ^{222}Rn to grow into secular equilibrium. Samples were counted in a high-purity, well-type Ge detector for ^{226}Ra (352 keV) and ^{228}Ra (911 keV). Detectors were calibrated using NIST-certified reference materials of the same sample geometry.

Sediments

^{224}Ra and ^{228}Th in wet bulk sediments were determined following the procedure of Cai et al. (2012). In the laboratory,

Ra-free Milli-Q water was added to each sediment container to form a slurry, stirred and ultrasonicated for ~ 10 min. Several drops of concentrated NH$_3$*H$_2$O were added to change the slurry pH to 8.0–9.0. Subsequently, 1.0 mL of KMnO$_4$ (3.0 g L^{-1}) and 1.0 mL of MnCl$_2$ (8.0 g MnCl$_2$*4H$_2$O L^{-1}) were added to each slurry to form a MnO$_2$ precipitate, which adsorbs any dissolved ^{224}Ra present in the interstitial pore fluid or that would have desorbed from the slurry procedure. The sediment slurry was then vacuum-filtered onto a pre-weighed 142-mm 0.7-μm glass microfiber filter. Filtration was stopped once water droplets were no longer observed leaving the filter tubing, and often lasted for 20 min. Samples (≤ 30 g) were placed in individual counting chambers and purged for ~ 10 min in an air stream (open loop via RaDeCC pump) to reduce any excess moisture. Water/sediment ratios generally matched in situ field conditions (i.e., $> 50\%$) and Rn emanation was not sensitive to minor variations in moisture content. Sample moisture levels were maintained between counting sessions by gently spraying Ra-free Milli-Q water onto the sediment and stored in a humid environment.

Samples were counted on a RaDeCC system to determine the activity of surface exchangeable ^{224}Ra and sediment-bound ^{228}Th present on particle surfaces and within the sediment interstitial pore fluids (hereafter ^{224}Ra and ^{228}Th activities) via Rn emanation. This is different from bulk ^{228}Th activities measured via alpha and gamma spectrometry, which measures both near-surface and mineral lattice-bound ^{228}Th (and ^{224}Ra) pools. Sediment samples were generally counted within 8–12 h of collection to minimize the decay of the initial ^{224}Ra pool and subsequent ingrowth via ^{228}Th decay. Samples were re-measured ~ 8 and ~ 25 d after collection for ^{228}Th determination when ^{224}Ra would have grown into secular equilibrium with ^{228}Th, while the decay of the initial ^{228}Th would be negligible ($< 1\%$); ^{228}Th activities were calculated as the average of these two runs (Cai et al. 2015). Uncertainties were determined from counting statistics and included corrections for radioactive decay, chance coincidence counts, the detector background, and the detector efficiency. Detector efficiencies were determined by creating a replicate set of homogeneous marsh sediment standards (collected at marsh site 1 creek station), which were sequentially spiked with increasing amounts of a ^{232}Th tracer in equilibrium with ^{228}Th (50.41 dpm g^{-1}; 0–40.33 dpm; $n = 5$; Cai et al. 2012).

Marsh sediments from the radiochemical analyses were combusted in a muffle furnace at 450°C for 24 h and sediment loss-on-ignition was calculated from weight loss. Post-combustion dry mineral mass was used to determine ^{224}Ra and ^{228}Th activities (dpm g^{-1} dry mineral mass). Bulk density was calculated from loss-on-ignition measurements based on the mixing model of Morris et al. (2016). A subset of each core section was weighed and dried in an oven at 40°C overnight, and porosity was calculated from weight loss.

Statistical analysis

Linear regression analyses were performed to investigate if tidal creek ^{224}Ra, ^{226}Ra, and ^{228}Ra activities varied as a function of creek water elevation and water quality variables (temperature, salinity, pH, DO). Two-tailed *t*-tests assuming unequal variance were performed to test the null hypothesis that means of various populations were statistically similar (α = 0.05). Tests were performed to compare (1) DIC concentrations, Ra activities, and ratios between marsh pore waters and brackish groundwaters; (2) DIC concentrations, Ra activities, and ratios between marsh sites 1 and 2; (3) sediment ^{224}Ra and DIC fluxes over different seasons and over (4) different marsh zones (creek, mid, interior). A previously developed hydrodynamic model was used to correct the current profiler data for overland flow (Wang et al. 2016). Calibrated YSI sensor data were used to calculate high-resolution (10-min intervals) tidal creek DIC concentrations using the multiple linear regression models developed by Wang et al. (2016) and Chu et al. (2018), for high-resolution DIC flux determination over the same time period integrated by the ^{224}Ra : ^{228}Th method.

Flux calculations

^{224}Ra : ^{228}Th disequilibria

The flux of ^{224}Ra across the sediment–water interface can be estimated from a one-dimensional vertical mass balance exchange model (Cai et al. 2012, 2014):

$$F_{Ra} = \int_0^\infty \lambda_{224}(A_{Th} - A_{Ra})\,dz \qquad (1)$$

where F_{Ra} is the flux of ^{224}Ra (positive upwards) across the sediment–water interface (dpm cm^{-2} d^{-1}), λ_{224} is the ^{224}Ra decay constant (0.189 d^{-1}), A_{Th} and A_{Ra} are the ^{228}Th and ^{224}Ra activities per unit volume of bulk sediments (dpm cm^{-3}) and dz is the total depth of integration (cm). The terms A_{Th} and A_{Ra} are converted from units of dpm g^{-1} to dpm cm^{-3} by correcting for sediment grain density (ρ_s; 2.65 g cm^{-3}) and porosity (φ) for each core subsection, where [dpm cm^{-3} = dpm g^{-1} × p_s × (1 − φ)] (Shi et al. 2019). The steady-state mass balance exchange model assumes that ^{224}Ra is only produced by the in-situ decay of ^{228}Th from the equivalent sediment depth horizon (i.e., no external sources or processes influencing the ^{224}Ra distribution) and that post-depositional mobilization of ^{228}Th is negligible. The ^{224}Ra flux is determined by trapezoidal integration across the depth at which ^{224}Ra : ^{228}Th disequilibrium occurs, until some depth at which ^{224}Ra and ^{228}Th reach secular equilibrium (activity ratio between 0.9 and 1.1; Cai et al. 2014). In multilayered systems (e.g., peat overlying a sandy aquifer), disequilibrium at depth may be interpreted from a one-dimensional horizontal mass balance exchange model, thereby taking the same form as Eq. 1 (Shi et al. 2019).

Interfacial and deep ^{224}Ra fluxes are used to constrain the volume of marsh pore water exchange over specific depth horizons,

$$Q = \frac{F_{Ra}}{A_{marsh} - A_{creek}} \qquad (2)$$

where A_{marsh} and A_{creek} represent the mean ^{224}Ra activity in the marsh pore water (depth specific) and tidal creek, respectively, and Q is marsh pore water exchange (L m^{-2} d^{-1}) (Shi et al. 2019). In this study, the distinction between interfacial and deep ^{224}Ra flux is inferred based on anticipated characteristics of tidal marsh hydrogeology, including vertical exchange within the shallow root zone (0–10 cm) and lateral flux at depth driven by hydraulic gradients, rather than based on distinct sediment layers (Shi et al. 2019). Interfacial and deep DIC fluxes are calculated by multiplying Q by the mean DIC concentration over the same depth interval corrected for seawater DIC concentration (i.e., net enrichment).

Tidal creek end-member mixing model

A three-end-member mixing model is used to constrain the relative proportions of ^{224}Ra and ^{226}Ra supplied by the coastal ocean (f_O), marsh pore water (f_M) and brackish groundwater (f_{GW}) to the tidal creek (Ra$_{creek}$) of Sage Lot Pond:

$$f_O + f_M + f_{GW} = 1 \qquad (3)$$

$$^{224}Ra_O \times f_O + {}^{224}Ra_M \times f_M + {}^{224}Ra_{GW} \times f_{GW} = {}^{224}Ra_{creek} \qquad (4)$$

$$^{226}Ra_O \times f_O + {}^{226}Ra_M \times f_M + {}^{226}Ra_{GW} \times f_{GW} = {}^{226}Ra_{creek} \qquad (5)$$

where Ra$_{creek}$ represents the observed ^{224}Ra and ^{226}Ra activity within the tidal creek at any given measurement period. Radioactive decay of ^{224}Ra is not included in 4 because the time scales of exchange here are near-instantaneous. This system of simultaneous equations is solved for f_o, f_M, and f_{GW} following Moore (2003). Marsh pore water exchange and brackish submarine groundwater discharge are calculated for each tidal cycle by multiplying the relative fraction of marsh pore water (f_M) or brackish groundwater (f_{GW}) within the tidal creek at each position of the tidal cycle by the instantaneous discharge of the tidal creek over the same time period (determined from current profiler measurements), and subsequently averaged over the duration of the tidal cycle.

Results

Pore waters

Marsh pore waters at sites 1 and 2 were relatively saline ($\sim$ 27–33) and had a pH range of $\sim$ 6.2–6.7 throughout the peat interior, with no apparent seasonality (Fig. 2). At site 1, pore waters closest to the tidal creek were equivalent to seawater salinity but decreased in salinity below −70 cm elevation, where brackish (18), lower pH ($\sim$ 6.1) groundwater was found below the peat–sand interface (Fig. 2A,B). There was no evidence of reduced pore water salinities for site 2 (Fig. 2C). Pore water ^{224}Ra activities were elevated near the marsh surface ($\sim$ 800–1200 dpm 100 L^{-1}) and decreased in activity down to a depth of 20 cm. The highest ^{224}Ra activities were
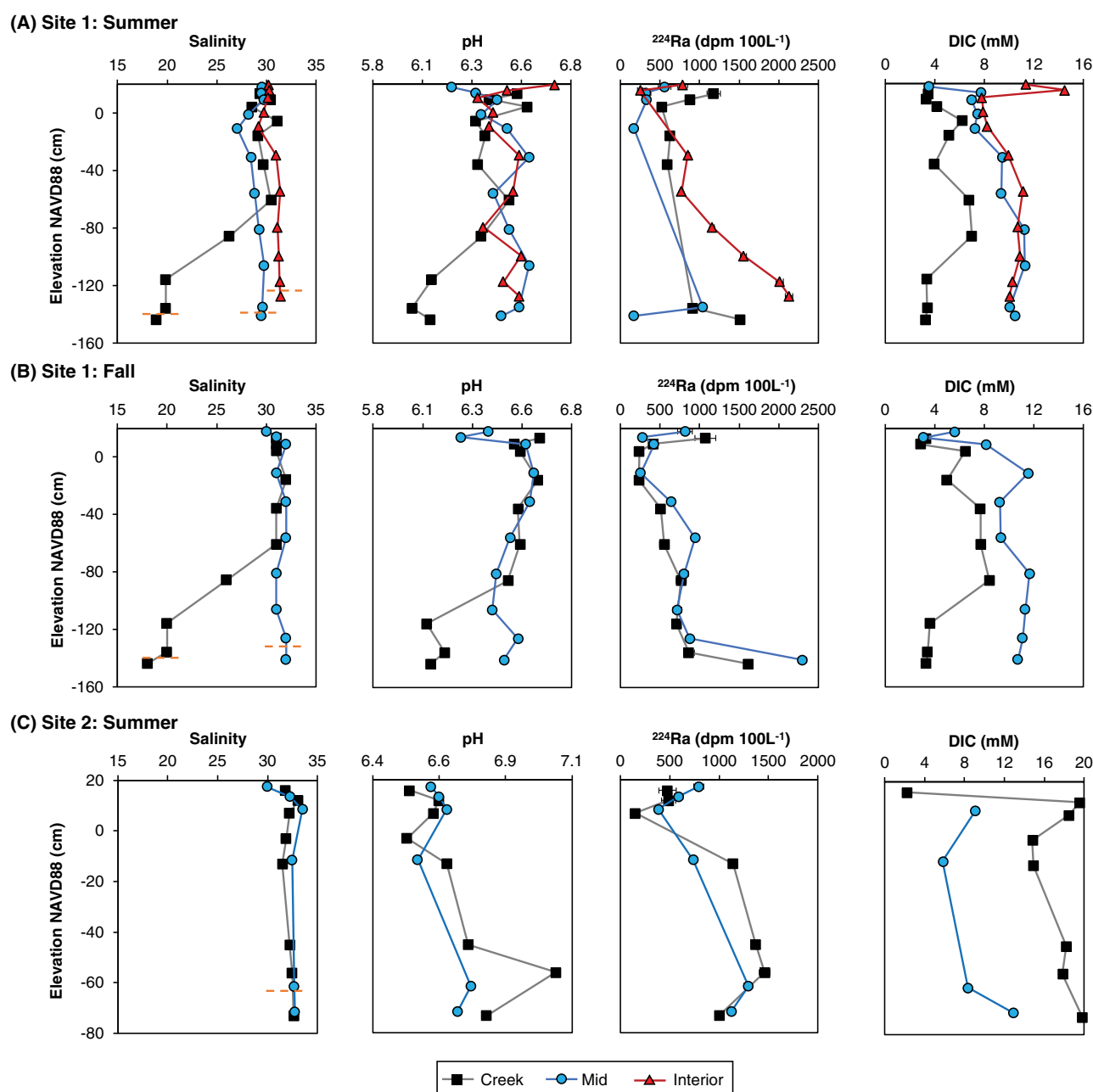
Fig. 2. Pore water profiles of salinity, pH, ^{224}Ra activity and dissolved inorganic carbon (DIC) concentration at marsh site 1 during summer (**A**) and fall 2019 (**B**), and at marsh site 2 during summer 2019 (**C**). The shallowest sample from each station was collected at 1 cm depth, just below the marsh surface. The dashed orange lines in the salinity panels represent the peat–sand interface. Note that the *x* and *y* axes in (**C**) differ from panels (**A**) and (**B**). Note that the interior station was not sampled during fall at site 1 (**B**) or during summer at site 2 (**C**).

observed near the peat-sand interface for brackish (1300–1500 dpm 100 L^{-1}) and saline ($\sim$ 1800–2120 dpm 100 L^{-1}) groundwaters (Fig. 2), although ^{224}Ra activities were not statistically different between marsh pore waters and brackish groundwaters ($p > 0.05$). Brackish groundwaters were enriched in long-lived ^{226}Ra and ^{228}Ra over marsh pore waters by a factor of five and two, respectively (Table 1). As a result, brackish groundwaters were markedly lower in ^{224}Ra/^{226}Ra (4.8 ± 1.0)

and ^{228}Ra/^{226}Ra (3.8 ± 0.2) compared to marsh pore waters (^{224}Ra/^{226}Ra $= 21.2 \pm 3.8$ and ^{228}Ra/^{226}Ra $= 10.8 \pm 1.7$; $p < 0.01$). Marsh pore water ^{224}Ra activities were not statistically different between marsh sites 1 and 2.

Marsh pore water DIC concentrations generally increased with increasing distance away from the tidal creek (Fig. 2). Shallow pore waters (1–10 cm) were largely elevated over tidal creek DIC concentrations for all stations and seasons

Table 1. Summary of marsh pore water and brackish groundwater end-members collected during 2019 and analyzed for ^{224}Ra, ^{226}Ra, ^{228}Ra (dpm 100 L^{-1}) and dissolved inorganic carbon (DIC) (mM). Depth = cm below marsh surface. Station IDs "1" and "2" represent marsh sites 1 and 2. Na = not analyzed.

Station ID	Date	Depth	Salinity	pH	DIC	^{224}Ra	^{226}Ra	^{228}Ra	^{224}Ra/^{226}Ra
Marsh pore water									
1-Creek	17 Jun	30	29	6.37	5.2	626	42	287	14.8
1-Mid	10 Jul	10	30	6.43	7.0	331	26	124	12.7
1-Interior	17 Jul	50	31	6.54	9.9	851	35	457	24.2
1-Interior	17 Jul	120	31	6.55	10.9	1556	31	732	49.9
1-Interior	17 Jul	148	31	6.54	10.0	2129	69	921	31.0
2-Creek	22 Jul	10	32	6.58	18.4	151	Na	221	Na
2-Creek	22 Jul	30	32	6.63	14.9	1141	46	613	25.0
2-Creek	22 Jul	90	33	6.78	19.8	1002	73	601	13.7
2-Mid	24 Jul	30	33	6.52	5.8	737	30	410	24.5
1-Creek	5 Nov	30	32	6.63	5.0	233	33	180	7.1
1-Creek	5 Nov	75	31	6.54	7.7	553	64	391	8.6
Average			31.4	6.56	10.4	846	45	449	21.2
Standard Error			0.3	0.03	1.5	171	5	71	3.8
Brackish groundwater									
1-Creek	18 Jun	150	20	6.00	3.4	914	153	554	6.0
1-Creek	18 Jun	158	19	6.09	3.2	1510	186	777	8.1
1-Creek	5 Nov	130	20	6.07	3.6	623	181	581	3.4
1-Creek	5 Nov	150	20	6.16	3.4	637	368	1253	1.7
1-Creek	5 Nov	158	18	6.09	3.3	1321	277	1277	4.8
Average			19.4	6.08	3.4	1001	233	888	4.8
Standard Error			0.4	0.02	0.1	160	35	142	1.0

(1.7–11.4 mM; Table 2). Deep pore water (> 10 cm depth) DIC concentrations were significantly higher (2.5–19.2 mM) than shallow pore waters. Marsh site 2 pore water DIC concentrations were approximately twofold greater than marsh site 1 ($p < 0.01$) reaching 19 mM (Fig. 2C). Brackish groundwaters were significantly lower in DIC concentration (3.4 ± 0.1 mM) compared to marsh pore waters ($p < 0.01$; Table 1). All pore water parameters (salinity, pH, ^{224}Ra, DIC) are summarized in an accompanying data release (Tamborski 2020).

Sediment cores

Sediment cores of various depths were collected between winter 2018 and fall 2019 at two marsh sites. Dry bulk density ($\sim$ 0.1–0.2 g cm^{-3}) did not significantly vary with depth or location within the marsh peat for either site; dry bulk density was between 0.90 and 1.02 g cm^{-3} for coarser-grained sediments collected at or below the peat–sand interface (site 2 mid station; Tamborski 2020). Surface-exchangeable ^{224}Ra and surface-bound ^{228}Th activities were generally highest near the marsh surface ($\sim$ 2–10 dpm g^{-1}) and rapidly decreased from 1 to $\sim$ 7 cm, reaching relatively constant activities from $\sim$ 7 to 50 cm depth (Figs. 3, 4). The relatively high ^{228}Th at the marsh surface can be attributed to the recent deposition of Th-rich sediments; the decrease in activity from 1 to $\sim$ 7 cm

reflects the natural radioactive decay of this particle-bound ^{228}Th ($t_{1/2}$ = 1.91 y).

In general, ^{224}Ra deficits relative to its parent ^{228}Th were observed within the upper 2 to 5 cm of the marsh surface, indicating the recent mobilization and transport of ^{224}Ra (e.g., Fig. 3C). Just below this shallow zone, ^{224}Ra : ^{228}Th activity ratios were generally within 0.9–1.1, here defined as secular equilibrium (1.0 ± 0.1 accounting for the analytical uncertainty of the measurements, determined from the standard deviation of the activity ratio uncertainties n = 196; Tamborski 2020). Winter 2018 cores collected at mid and interior stations were notable exceptions, where activity ratios < 0.9 were found at discrete depth horizons, and in the case of marsh site 2 (mid), throughout the entire shallow core (0–25 cm; Table 2).

Sediment cores that spanned the full depth of the peat (0–150 cm) at marsh site 1 (summer and fall 2019) revealed mid-depth and near bottom-depth maxima of ^{224}Ra and ^{228}Th activities (Figs. 3, 4); there was no discernable difference in bulk density at these depth horizons (Tamborski 2020). During summer 2019, large activity ratio deficits were found for the creek (0.75 ± 0.07), mid (0.38 ± 0.04) and interior (0.82 ± 0.12) core stations between − 20 and − 40 cm elevation, with an additional activity ratio deficit (0.45 ± 0.04 to 0.68 ± 0.07) between − 75 and − 85 cm for the creek station

Table 2. Summary of pore water ^{224}Ra and dissolved inorganic carbon (DIC) concentrations and fluxes determined from ^{224}Ra : ^{228}Th measurements. Interfacial and deep depth ranges correspond to integrated depth zones where ^{224}Ra : ^{228}Th activity ratios < 0.9. n/a = flux not observed. Station ID "1" and "2" represent marsh sites 1 and 2.

Station ID	Shallow pore water			Deep pore water			Interfacial (surface)		Diffusion	Deep (lateral)	
	Depth cm	^{224}Ra dpm L^{-1}	DIC mM	Depth cm	^{224}Ra dpm L^{-1}	DIC mM	Depth range cm	^{224}Ra flux dpm cm^{-2} d^{-1}	^{224}Ra flux dpm cm^{-2} d^{-1}	Depth range cm	^{224}Ra flux dpm cm^{-2} d^{-1}
Winter 2018											
1-Creek	10	4.9 ± 0.3	1.9	30	5.4 ± 0.6	8.7	0–3	0.05 ± 0.02	0.002	n/a	n/a
1-Mid	10	3.3 ± 0.3	3.8	30	3.8 ± 0.3	8.6	0–4	0.05 ± 0.02	0.002	n/a	n/a
1-Interior	10	1.4 ± 0.1	2.8	20	3.2 ± 1.0	5.5	0–2	0.00 ± 0.02	0.008	8–24	0.19 ± 0.03
2-Creek	10	4.7 ± 0.2	4.9	30	6.4 ± 0.9	19.2	0–7	0.09 ± 0.04	0.002	n/a	n/a
2-Mid	10	3.2 ± 0.2	8.7	30	2.6 ± 0.4	16.8	0–4	0.02 ± 0.01	0.001	6–24	0.10 ± 0.02
2-Interior	10	2.5 ± 0.1	9.6	20	2.6 ± 0.4	12.8	0–3	0.08 ± 0.01	0.009	6–24	0.12 ± 0.02
Spring 2019											
1-Creek	1	2.2 ± 0.5	1.7	30	4.0 ± 0.4	2.5	0–4	0.22 ± 0.02	0.030	n/a	n/a
1-mid	1	1.4 ± 0.3	2.3	30	4.2 ± 0.4	4.0	0–4	0.03 ± 0.01	0.002	n/a	n/a
Summer 2019											
1-Creek	5	8.8 ± 0.4	3.3	150	9.9 ± 0.2	5.7*	0–7	0.20 ± 0.03	0.025	36–110	0.58 ± 0.23
1-Mid	1	5.6 ± 0.8	3.5	154	10.4 ± 0.5	8.7*	0–3	0.13 ± 0.01	0.025	36–69	0.55 ± 0.09
1-Interior	1	7.9 ± 0.6	11.4	138	20.1 ± 0.4	10.0*	0–2	0.03 ± 0.01	0.005	27–107	0.62 ± 0.25
2-Creek	1	4.8 ± 0.9	2.2	73	14.6 ± 0.5	17.8	0–2	0.00 ± 0.02	0.001	n/a	n/a
2-Mid	1	7.9 ± 0.5	—	80	13.0 ± 0.5	9.0*	n/a	n/a	n/a	17–85	0.32 ± 0.17
Fall 2019											
1-Creek	1	10.7 ± 1.3	3.3	50	5.1 ± 0.1	8.0*	0–3	0.05 ± 0.03	0.004	43–97	0.10 ± 0.15
1-Mid	1	8.2 ± 1.0	5.6	125	7.2 ± 0.6	11.4*	0–3	0.02 ± 0.06	0.002	117–137	0.22 ± 0.21

*Average pore water DIC concentration over given depth range.

(Fig. 3). These same depth horizons were observed to have an activity ratio less than 0.9 during fall 2019; however, the activity ratios were relatively higher (0.78 ± 0.13 minimum at − 30 cm and 0.87 ± 0.10 minimum at − 75 cm), suggesting less Ra transport in the fall compared to the summer (Fig. 4). At marsh site 2, activities of ^{224}Ra and ^{228}Th were relatively uniform with depth within the marsh peat below 10 cm (~ 0.7–1.7 dpm g^{-1}) and were lowest below the peat-sand interface (0.2–0.3 dpm g^{-1}; Fig. 4). Unlike marsh site 1, mid-depth and bottom-depth activity maxima were not observed. All sediment samples collected near the peat–sand interface were in secular equilibrium between ^{224}Ra and ^{228}Th, for both marsh sites and seasons. All cores and the relative depth ranges where activity ratio deficits were observed are summarized in Table 2; raw core data are summarized in an accompanying data release (Tamborski 2020).

Radium flux and pore water exchange

Sediment core ^{224}Ra : ^{228}Th disequilibria is used to determine seasonal pore water exchange and DIC flux. This method integrates over a period of ~ 10 d, and is thus ideal to integrate DIC transport over multiple tidal cycles.

Critically, this method allows us to resolve the location, that is, relative to tidal creeks, as well as the depth within the peat subsurface, where pore water exchange occurs. Here, we use Eq. 1 to derive ^{224}Ra fluxes within the upper 10 cm of the marsh surface (designated as "interfacial"); note that this depth interval is arbitrary and interfacial exchange is simply based on the integration of the shallow ^{224}Ra : ^{228}Th activity ratio deficits observed for each core within the rhizosphere (Table 2). Deficits below 10 cm are interpreted as the mobilization and transport of Ra due to lateral advection (designated as deep pore water exchange). Profiles of ^{224}Ra and ^{228}Th were integrated over specific depth intervals where activity ratios were < 0.9 and are summarized in Table 2. Molecular diffusion of ^{224}Ra is estimated from Fick's first law at each station using the concentration gradient between shallow surface-exchangeable ^{224}Ra (0–1 cm) and the concentration of ^{224}Ra in the tidal creek at high tide for each sampling period (Table 3), corrected for temperature and tortuosity (Cai et al. 2014). Molecular diffusion generally accounted for < 10% of the interfacial ^{224}Ra flux, signifying that advection is the primary mechanism of interfacial ^{224}Ra transport (Table 2).
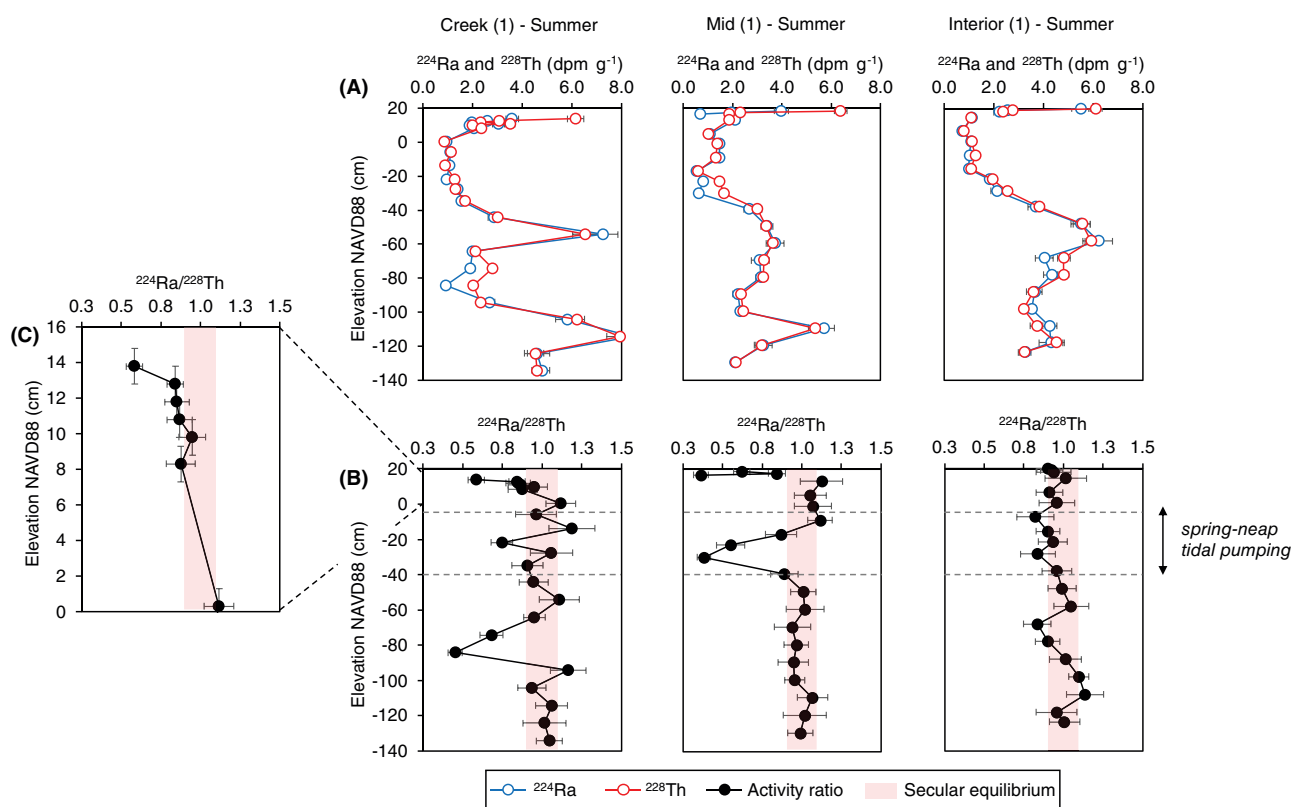
Fig. 3. Summer 2019 distribution of surface-exchangeable ^{224}Ra and sediment-bound ^{228}Th (**A**) and corresponding activity ratios (**B**) for site 1. Panel (**C**) is a zoomed in view of the creek station activity ratio. Pink shading indicates secular equilibrium (0.9–1.1). Horizontal dashed gray lines represent the approximate elevation range corresponding to low tide.

At marsh site 1, mean ($\pm$ SD) interfacial ^{224}Ra fluxes were generally highest near the creek bank (0.13 ± 0.08 dpm cm^{-2} d^{-1}; n = 4) and decreased towards the marsh interior ("mid" = 0.06 ± 0.04 dpm cm^{-2} d^{-1}; n = 4; Table 2). This decrease broadly reflects the tidal inundation period of each station with respect to absolute elevation (Fig. 5; Table S1). Tidal inundation was calculated as the percent of time water levels were greater than marsh platform elevation over the 10–14-day period prior to core collection at each marsh sampling site. Flooding frequency was greatest both in the summer, associated with higher water levels, and at lower marsh elevation. Interfacial ^{224}Ra exchange increased sharply once flooding reached more than 20% (Fig. 5).

Deep ^{224}Ra fluxes generally exceeded interfacial fluxes by a factor of 2–20-in cores where activity ratio deficits were observed (Table 2). Deep ^{224}Ra fluxes (full-peat cores) during the summer were greater than the fall (p = 0.048; Table 2). Seasonal changes in ^{224}Ra distributions and fluxes may be driven by processes that are not hydrologic. Sulfate reduction may increase the solubility of Mn and Fe oxides scavenged to sediment surfaces, thereby releasing dissolved Ra to the surrounding pore waters (Bollinger and Moore 1993). At Sage Lot Pond, redox potential and pH do not show any statistically significant relationship with pore water Ra activity (e.g., Fig. 2),

suggesting that pore water Ra distributions are primarily impacted by changes in hydrology.

Deep, lateral pore water exchange (20–80 L m^{-2} d^{-1}) is significantly greater than interfacial pore water exchange (0–36 L m^{-2} d^{-1}) at both marsh sites, for all seasons (range in values derived from Eq. 2; Fig. 6A). Winter 2018 cores only extended to 25 cm and are therefore lower bound, conservative estimates. Area-normalized fluxes are upscaled to absolute fluxes (m^3 d^{-1}) using surface elevation (interfacial Q) and lateral distance from the tidal creek (deep Q; Supporting Information). Flushing of the creek station (site 1) at depth during summer accounted for 55% of the total marsh pore water exchange, with decreasing contributions from the mid (33%) and interior (13%) marsh zones, though creek and mid stations were equivalent during the fall. Marsh pore water exchange was comparable between sites 1 and 2 during winter 2018 but was lower at site 2 during summer 2019, when no flux was observed for the creek station (Fig. 6A).

DIC export

Spatial variability in marsh pore water exchange drives variability in DIC flux (Fig. 6B). At marsh site 1, interfacial and deep DIC fluxes varied from 0.0 to 0.7 and 1.7–5.4 g C m^{-2} d^{-1}, respectively. Deep pore water DIC concentrations at site
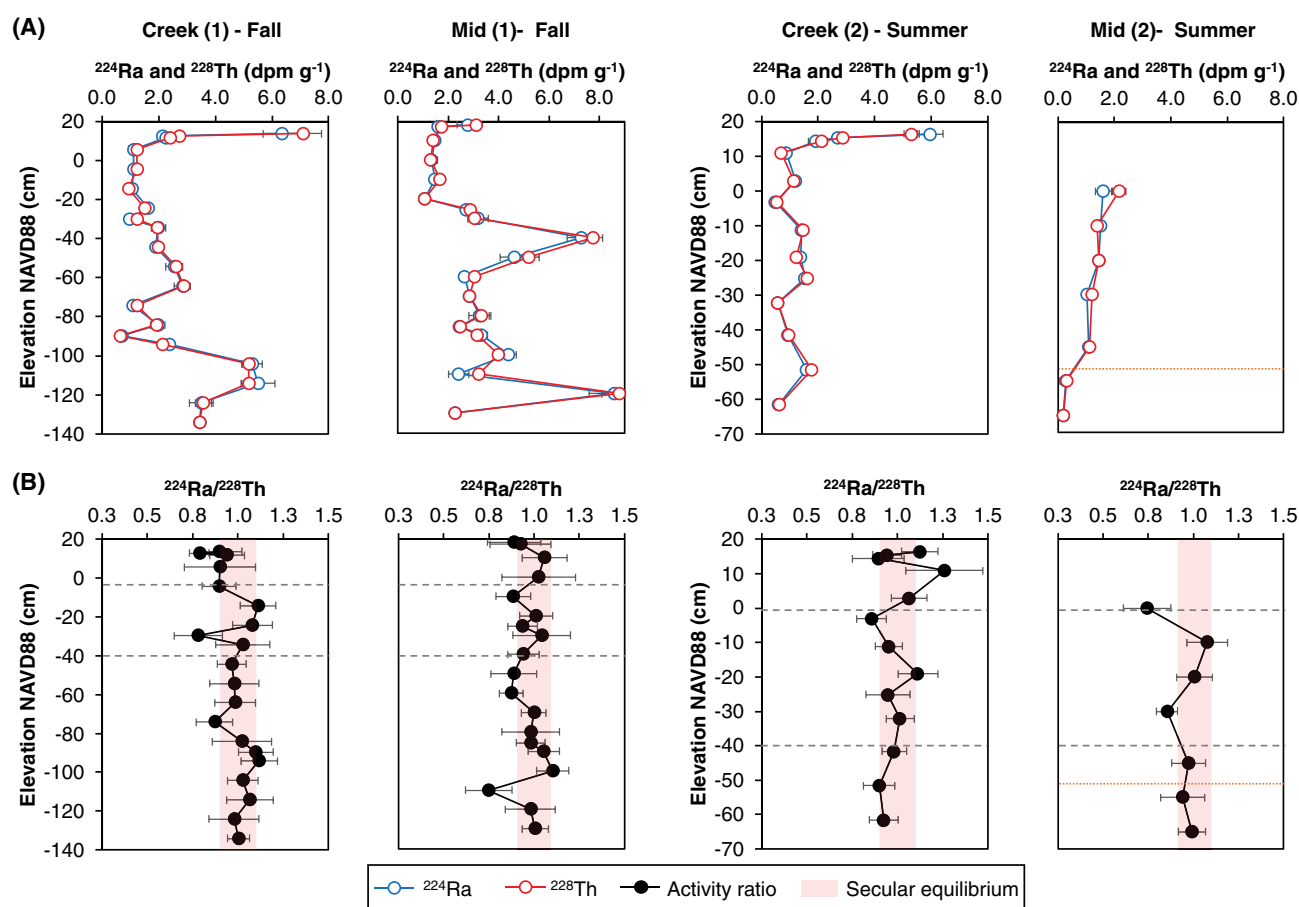
Fig. 4. Site 1 (fall 2019—left) and site 2 (summer 2019—right) distribution of surface-exchangeable ^{224}Ra and sediment-bound ^{228}Th (**A**) and corresponding activity ratios (**B**). Pink shading indicates secular equilibrium (0.9–1.1). Note the *y*-axis scales for sites 1 and 2 are different. Shallow sediments (> 0 cm) from the mid station (site 2) are not included and the peat–sand interface is indicated by an orange line. Horizontal dashed gray lines represent the elevation range corresponding to low tide.

2 were nearly twice that of site 1 (Table 2), resulting in significantly higher deep DIC fluxes (9.1–10.1 g C m^{-2} d^{-1}; *p* < 0.01) during winter 2018.

Scaled to drainage basin area, deep pore water exchange supplied 79–94% of the total DIC exported to the tidal creek at marsh site 1 (2.7 × 10^3 to 15.4 × 10^3 g C d^{-1}), with minor contributions from interfacial pore water exchange (0.4 × 10^3 to 2.5 × 10^3 g C d^{-1}). Importantly, creek and mid stations sustained a nearly equivalent DIC flux (Fig. 7) that must primarily be derived from the marsh sediment depth horizon intersected by mean low tide (Figs. 3, 4). Interfacial DIC export was primarily derived from low marsh elevation zones (creek and mid stations; Fig. 7). Upscaled to the entire drainage basin (site 1), area-normalized DIC fluxes (interfacial + deep) were lowest during winter (0.8 ± 0.3 g C m^{-2} d^{-1}), slightly higher during fall (1.4 ± 1.1 g C m^{-2} d^{-1}) and highest during summer (4.3 ± 0.8 g C m^{-2} d^{-1}). These three seasonal estimates result in an annual average flux of 790 ± 560 g C m^{-2} y^{-1} for marsh site 1 (excluding the spring); a lack of complete seasonal data

prevents estimating an average annual DIC flux for marsh site 2.

Tidal time series

A total of 17 discrete tidal cycles were sampled between 2015 and 2019 encompassing a range of tidal water elevations (Table 3). Mean higher high water for Sage Lot Pond is 0.2 m (Gonneea et al. 2019); we use this threshold as the lower limit for "spring tides." A total of 9 spring tides were sampled in 2015, 2016, and 2019 (Table 3). In general, ^{224}Ra (54–811 dpm 100 L^{-1}) displayed a wider range in activity over individual tidal cycles compared to long-lived ^{226}Ra (13–90 dpm 100 L^{-1}) and ^{228}Ra (44–314 dpm 100 L^{-1}; Fig. 8A,B). Long-lived Ra activities were generally highest at intermediate salinities (∼ 22), while maximum ^{224}Ra activities were observed at salinities close to background seawater (∼ 27–31). All Ra isotopes were inversely correlated with tidal creek water levels (*p* < .01; Fig. 8A).

Table 3. Summary statistics for discrete tidal cycles at marsh site 1.

Tidal cycle #	Date	Elevation (m NAVD88)			^{224}Ra (dpm 100 L^{-1})			^{226}Ra (dpm 100 L^{-1})			^{228}Ra (dpm 100 L^{-1})			n
		Min	Mean	Max	Min	Mean	Max	Min	Mean	Max	Min	Mean	Max	
1	17 Apr 2015	−0.40	−0.21	0.05	110	177	309	35	57	90	126	207	314	10
2	30 Apr 2015	−0.23	−0.08	0.05	75	115	153	22	28	35	89	105	126	10
3	21 Jul 2015*	−0.15	0.10	0.28	108	166	256	38	43	57	157	183	234	10
4	30 Jul 2015	−0.29	−0.10	0.06	194	221	267	43	49	57	182	204	238	9
5	7 Oct 2015*	−0.08	0.11	0.25	114	138	180	27	31	34	91	113	138	10
6	27 Oct 2015*	−0.29	−0.01	0.28	110	183	311	17	27	38	83	116	168	10
7	9 May 2016	−0.23	−0.04	0.15	136	218	387	26	32	43	96	123	160	7
8	25 May 2016	−0.25	−0.07	0.12	122	267	357	28	41	49	108	158	199	7
9	12 Jul 2016	−0.27	−0.12	0.03	215	394	722	39	48	63	148	202	281	9
10	26 Jul 2016*	−0.17	0.05	0.29	204	344	554	36	44	57	150	178	237	8
11	18 Oct 2016*	−0.16	0.28	0.58	126	213	373	24	29	39	94	114	148	8
12	1 Nov 2016*	−0.10	0.10	0.24	92	184	301	24	27	31	90	105	126	9
13	9 May 2019	−0.27	−0.10	0.08	105	202	396	18	24	29	61	96	136	10
14	16 May 2019	−0.32	−0.06	0.17	106	164	254	18	21	26	61	76	102	10
15	12 Jun 2019*	0.05	0.28	0.51	185	374	811	20	28	37	70	112	171	10
16	10 Jul 2019*	−0.18	0.09	0.30	193	275	528	22	26	33	78	99	136	10
17	30 Oct 2019*	−0.15	0.20	0.49	54	105	157	13	15	17	44	52	62	9

*Denotes spring tides, for which the maximum water elevation is ≥ 0.2 m (mean higher high water).
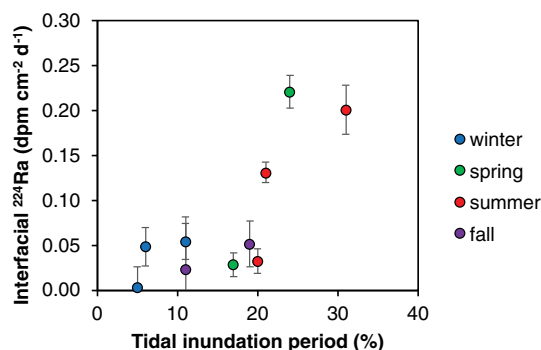

Fig. 5. Interfacial ^{224}Ra fluxes (0–5 cm) versus tidal inundation period (% of tidal period flooded) for marsh site 1, arranged by season.

The tidal cycles sampled between 2015 and 2019 at marsh site 1 are used to determine seasonal and annual variation in marsh pore water exchange and thus DIC flux. In the Ra end-member mixing model (Eqs. 3–5), the coastal ocean end-member is simply set as the lowest tidal creek ^{224}Ra and ^{226}Ra activity observed (near high tide; Table 3) for each discrete tidal cycle. Marsh pore water and brackish groundwater end-members are taken as the averages reported in Table 1 for all seasons and therefore, we assume that Ra end-member activities do not vary annually (Fig. 9). An example of the three-end-member mixing model is presented in Fig. 8D. Over this July 2019 tidal cycle, Ra activities were lowest at high tide and increased in activity with decreasing water elevation (Fig. 8C). The maximum ^{224}Ra activity at ebb tide (528 dpm 100 L^{-1})

can be explained by approximately equal proportions of sea-water (49%; *f-sea*) and marsh pore water (51%; *f-marsh*) mixing within the tidal creek. The fact that the peak Ra contribution does not occur at low tide suggests that the hydrogeologic response of the marsh platform is complex and not simply represented by ebb-flood tidal dynamics. Annual average (± SE) marsh pore water exchange was lowest during 2015 (14 ± 6 L m^{-2} d^{-1}), a period characterized by relatively low sea levels, and increased from 2016 (26 ± 11 L m^{-2} d^{-1}) through 2019 (81 ± 36 L m^{-2} d^{-1}) as sea level progressively increased (Fig. 10). Monthly mean sea level was significantly correlated to marsh pore water exchange ($r^2 = 0.60$, $p = 0.02$), excluding fall 2019 (the only sampling period represented by one tidal cycle).

Discussion

Model assumptions and sensitivity

The ^{224}Ra : ^{228}Th approach integrates over a 10-day period, thus encompassing multiple tidal cycles. While ^{224}Ra exhibits a "memory" effect in the sediments, the distribution of DIC will vary due to changes in marsh pore water exchange and the delivery of oxidants to the subsurface, as well as seasonality in microbial respiration. Therefore, an implicit assumption in the DIC flux calculations is that pore water DIC concentrations are in steady-state over the ^{224}Ra : ^{228}Th flux integration period. Pore water profiles collected between summer and fall at marsh site 1 are comparable, lending support to this assumption. A clear violation of this assumption is demonstrated by the pore water DIC profile at marsh site 2 that was
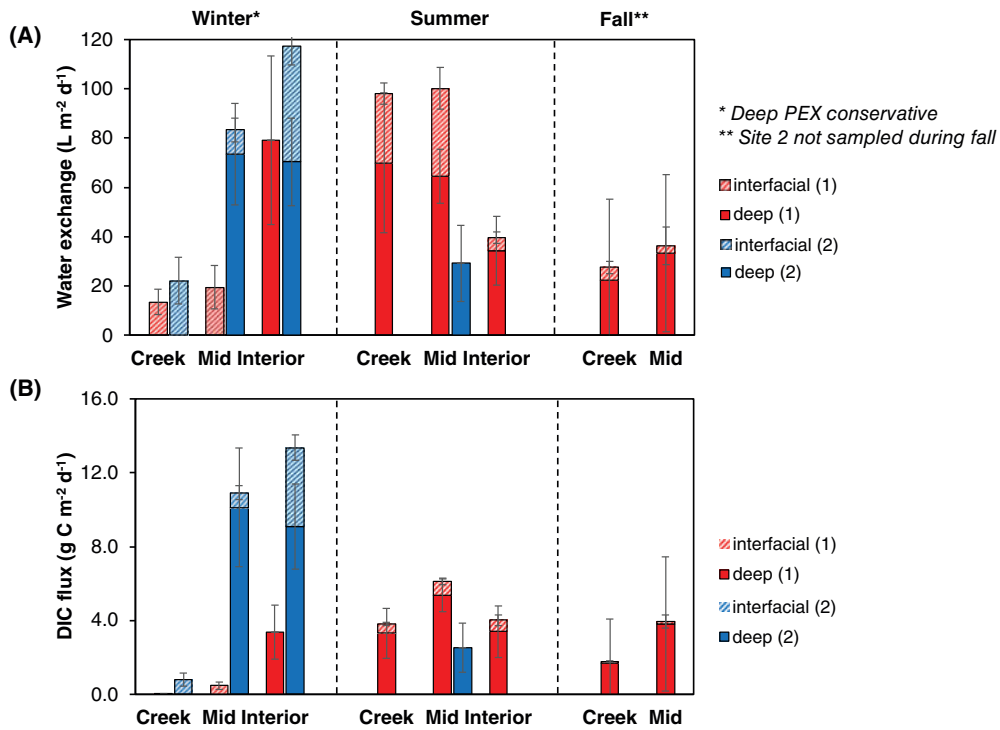
Fig. 6. Area-normalized interfacial and deep pore water exchange (PEX) (**A**) and dissolved inorganic carbon (DIC) (**B**) flux for different marsh zones determined from ^{224}Ra : ^{228}Th disequilibria at marsh site 1 (red) and marsh site 2 (blue). No flux was observed for marsh site 2 creek station during summer; the interior station was not sampled. *Note that deep pore water exchange for the winter creek and mid stations was not determined from these shallow (25 cm) cores and is therefore conservative estimates. **Marsh site 2 was not sampled during fall.
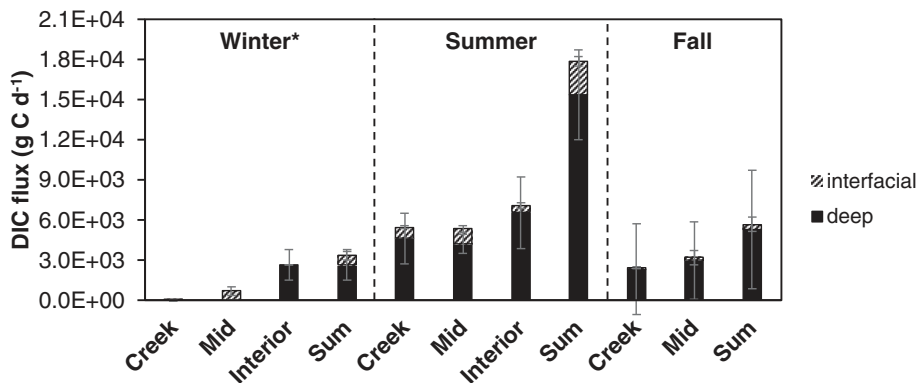
Fig. 7. Absolute interfacial and deep dissolved inorganic carbon (DIC) fluxes for different marsh zones determined from ^{224}Ra : ^{228}Th disequilibria at marsh site 1. Sum represents the total flux from all stations. *Note that deep pore water exchange for the winter creek and mid stations was not determined from these shallow (25 cm) cores and are therefore conservative estimates. The interior station was not sampled during fall.

collected after a moderate storm event ("mid" station; Fig. 2C) which had much lower DIC concentrations and associated instantaneous flux presumably due to a recent flushing event (Fig. 6A). Note that for interfacial fluxes, the Ra and DIC pore water end-members integrate over a maximum 1 cm sampling radius. Given that the shallow ^{224}Ra : ^{228}Th activity ratio deficits are generally deeper than 2 cm, the impact of a depth integrated pore water concentration on the estimated fluxes is likely minor.

Analytical uncertainties for dissolved ^{224}Ra ($\sim 5\%$) and ^{226}Ra ($\sim 3\%$) are minor in comparison to the natural variability of marsh pore water and brackish groundwater Ra activities. Natural variability in these end-members will inherently produce uncertainty in selecting end-members for the tidal mixing models (Eq. 3–5). The ^{224}Ra/^{226}Ra activity ratios of the marsh pore water and brackish groundwaters are distinct enough that minor changes in activity ratios are relatively

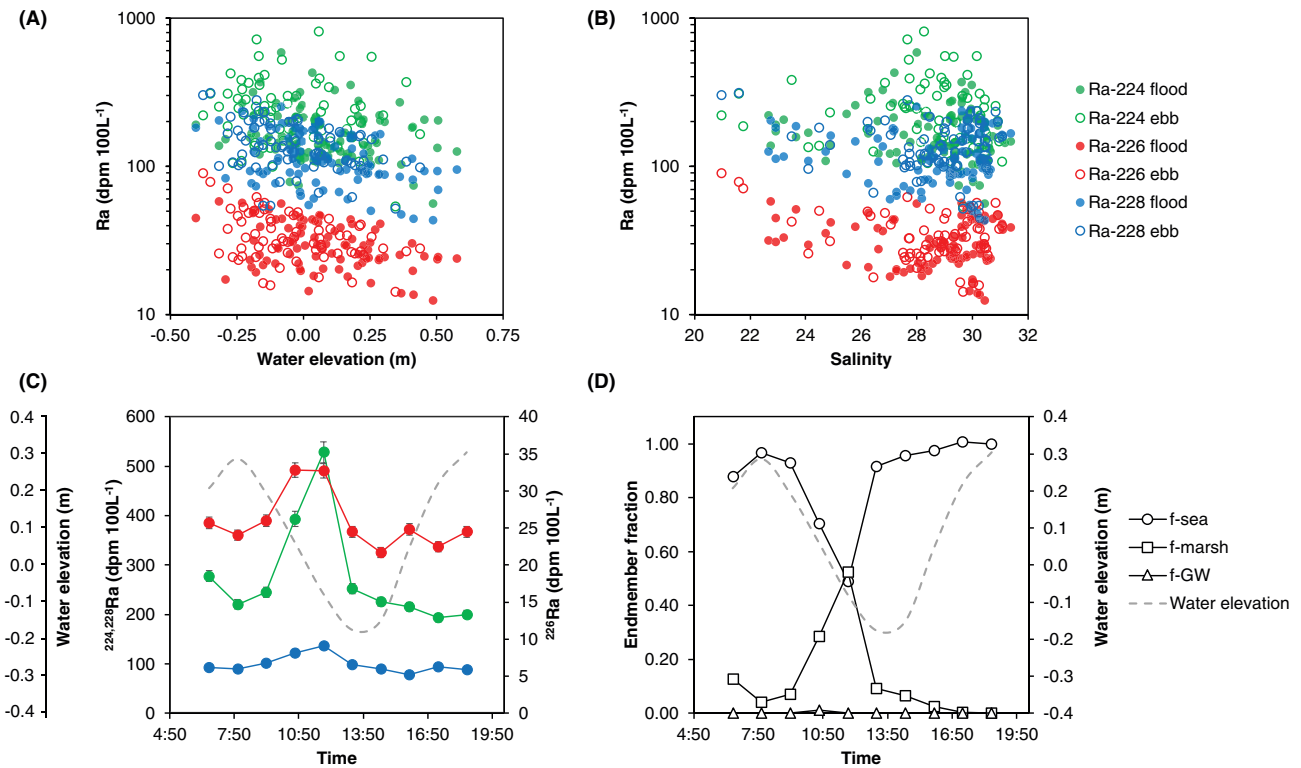**Fig. 8.** Tidal creek Ra isotope variation as a function of creek water elevation (**A**) and salinity (**B**) over 17 discrete tidal cycles (*n* = 156). Samples are classified as either flood tide (closed symbols) or ebb tide (hollow symbols). Hourly variation in Ra activity and creek water elevation during a July 2019 tidal cycle (**C**) with results of the ^{224}Ra/^{226}Ra end-member mixing model (**D**).
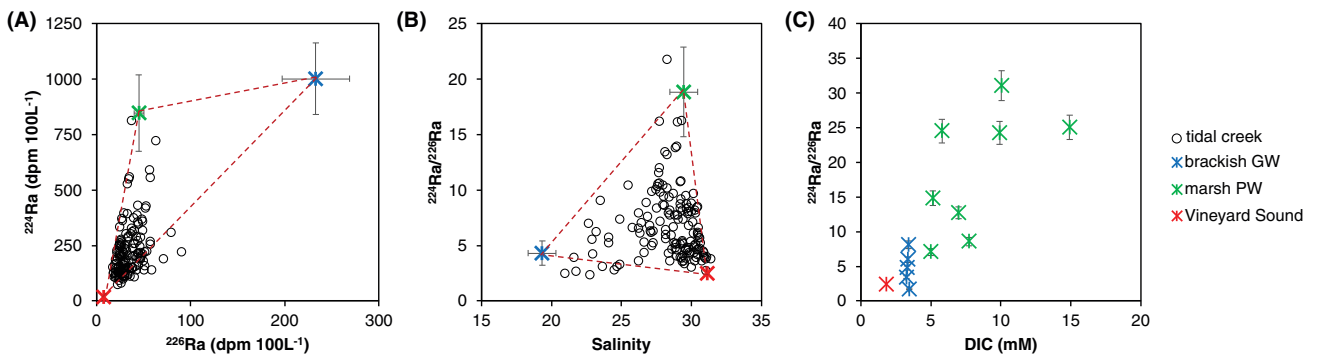

Fig. 9. Variation in ^{224}Ra versus ^{226}Ra (**A**), ^{224}Ra/^{226}Ra versus salinity (**B**) and versus dissolved inorganic carbon (DIC) concentration (**C**). Brackish groundwater and marsh pore water end-members in (**A**) and (**B**) represent the mean ($\pm$ SE) of the samples summarized in Table 1. The red dashed triangles represent the model domain of the three-end-member mixing model. The coastal ocean end-member is taken as the high tide measurement during each tidal cycle and Vineyard Sound is shown for comparison only.

insignificant in the end-member mixing model. For example, increasing the brackish groundwater ^{224,226}Ra activities by 25% results in, on average, no change in marsh pore water exchange and a 22% change in brackish submarine groundwater discharge, signifying that brackish groundwater is more sensitive to changes in long-lived ^{226}Ra. The coastal ocean end-member was set as the lowest Ra activity observed over each tidal cycle, typically measured at high tide. This

approach accounts for seasonal variation in flushing of the broader Waquoit Bay estuary with Vineyard Sound (e.g., Rama and Moore 1996). Setting Vineyard Sound as the coastal ocean Ra end-member results in, on average, only a 33% change in marsh pore water exchange. Ultimately, the mixing model is sufficient to resolve relative changes in pore water exchange and brackish groundwater discharge between individual tidal cycles.
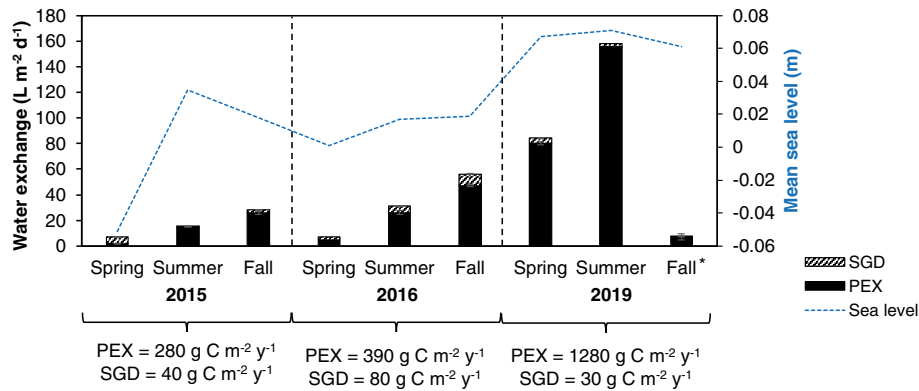
Fig. 10. Seasonal rates of marsh pore water exchange (PEX) and brackish submarine groundwater discharge (SGD) derived from the $^{224}Ra/^{226}Ra$ mixing model. Annual average dissolved inorganic carbon export for marsh PEX and brackish SGD are shown below each year. Each seasonal water exchange rate is the average of two tidal cycles, aside from fall 2019 (*one tidal cycle only). Monthly mean sea level data is from NOAA station 8447930 in Woods Hole, Massachusetts.

Flux magnitudes and comparison

The $^{224}Ra : ^{228}Th$ activity ratio deficits in sediment profiles should supply the excess ^{224}Ra activities observed in the tidal creek. Average tidal time-series pore water exchange estimates for the summer 2019 tidal cycles (156 L m^{-2} d^{-1}) are in agreement with pore water exchange determined from $^{224}Ra : ^{228}Th$ disequilibria (interfacial + deep = 150 ± 30 L m^{-2} d^{-1}) over the same period. Marsh pore water exchange determined from the tidal time series during November 2019 (7 L m^{-2} d^{-1}) is lower but not statistically different than area-normalized pore water exchange determined from $^{224}Ra : ^{228}Th$ disequilibria (14 ± 13 L m^{-2} d^{-1}) over the same period. Absolute differences in flux magnitude may be due to differences in the integration period of each method. The $^{224}Ra : ^{228}Th$ method integrates over a period of ~ 10 d, while the tidal time series captures near-instantaneous changes in flux. Overall, these two independent methods are in relative agreement and reasonably track changes in seasonal pore water exchange. Tide-induced pore water exchange at Sage Lot Pond is similar to intertidal marshes in North Inlet, SC (38–230 L m^{-2} d^{-1}; Bollinger and Moore 1993; Shi et al. 2019) and the nearby Pamet River Estuary, Massachusetts (43–54 L m^{-2} d^{-1}; Charette 2007).

Marsh pore water exchange determined from the tidal time series can be used to infer seasonal and annual changes in DIC export, given that end-member $^{224}Ra/^{226}Ra$ ratios reasonably track DIC concentrations. Marsh pore water DIC concentrations are relatively low during spring and increase during summer due to enhanced microbial respiration and plant activity from warmer air temperatures (Wang et al. 2016). DIC concentrations remain relatively high through the fall (Brooks et al. 2021; Table S2), likely as a consequence of respiration lagging production. These seasonal end-members are used to derive a net pore water enrichment concentration (corrected for a seawater DIC concentration of 2.0 mM) for estimating seasonal fluxes. To derive an annual average, we assume that each sampling period is representative of its corresponding 3-month season and further assume that there is zero DIC export during the winter (January–March; Wang et al. 2016). This is a clear oversimplification of the marsh system and only serves as a first-order estimation. This simple approach suggests that the annual average DIC export increased from 2015 (280 g C m^{-2} y^{-1}) to 2016 (390 g C m^{-2} y^{-1}) and 2019 (1280 g C m^{-2} y^{-1}). The absolute value of these DIC flux estimates should be cautiously interpreted; however, variability in seasonal and annual pore water exchange demonstrates that lateral DIC export may vary with sea level (Fig. 10), which has significant implications for future blue carbon storage (Guimond et al. 2020b).

Brackish submarine groundwater discharge, using a mean DIC end-member of 3.4 mM, supplies between 30 and 80 g C m^{-2} y^{-1}, similar to fresh groundwater discharge estimates (36 g C m^{-2} y^{-1}) from a salt balance (Wang et al. 2016). Note that annual average brackish groundwater fluxes represent an average of the three sampling seasons only. Marsh pore water exchange-driven DIC export exceeds brackish groundwater fluxes by an order of magnitude, demonstrating that brackish groundwater is a relatively insignificant DIC vector in this groundwater-impacted estuary.

Lateral DIC flux method comparisons including tidal creek DIC concentration modeling, Ra end-member mixing models, and $^{224}Ra : ^{228}Th$ disequilibria are summarized in Table 4. Note that because each method integrates over different spatial and temporal scales, direct comparison between methods is qualitative only. Tidal creek-based DIC flux estimates from 2012 to 2015 are in relative agreement with the DIC flux estimates determined from the tidal time series mixing model and $^{224}Ra : ^{228}Th$ disequilibria for 2018–2019. During winter 2018, the modeled tidal creek DIC flux (0.5 ± 0.05 g C m^{-2} d^{-1} between 08 December 2018 and 18 December 2018), based on the multiple linear regression model of Wang et al. (2016), was comparable to the DIC flux determined from $^{224}Ra : ^{228}Th$ disequilibria over the same integrated time period. The multiple

Table 4. Dissolved inorganic carbon flux method comparison at marsh site 1. CHANOS = CHANelized Optical Sensor, measured during 2015 (Chu et al. 2018). MLR = multiple linear regression tidal model, 2018–2019. Average seasonal and annual dissolved inorganic carbon flux from 2012–2014 is shown in parentheses for comparison, assuming zero export from January to March (Wang et al. 2016). 2018–2019 MLR fluxes integrate over an approximate time period equivalent to the $^{224}Ra : ^{228}Th$ Cores. Na = not available.

Time period	CHANOS (2015)	MLR tidal model	Ra mixing model	Ra:Th cores
	g C m^{-2} d^{-1}	g C m^{-2} d^{-1}	g C m^{-2} d^{-1}	g C m^{-2} d^{-1}
Winter	2.0	0.5 ± 0.05* (0.3)	Na	0.8 ± 0.3†
Spring	Na	Na (0.5)	1.9	0.1 ± 0.1†
Summer	3.0	1.0 ± 0.1* (1.4)	11.5	4.3 ± 0.8
Fall	Na	3.5 ± 0.4* (1.3)	0.5	1.4 ± 1.1
Annual (g C m^{-2} y^{-1})	Na	Na (414)	1280	790 ± 560

*Winter average from 08 December 2018 to 18 December 2018; Summer average from 09 July 2019 to 17 July 2019; Fall average from 29 October 2019 to 7 November 2019.
†Conservative estimate: winter = shallow cores; spring = interfacial flux only (mid station).

linear regression model underpredicted tidal creek DIC concentrations during summer 2019 (Fig. S1), and may thus partially explain why modeled fluxes were lower than the $^{224}Ra : ^{228}Th$ DIC flux during this period (1.0 ± 0.1 g C m^{-2} d^{-1} between 09 July 2019 and 17 July 2019). In contrast, modeled DIC concentrations during fall 2019 overpredicted DIC concentrations (Fig. S1); this is the only time period in which tidal creek-modeled DIC fluxes exceeded that of Ra-based approaches. High-resolution time-series monitoring of the main tidal channel in 2015 (CHANOS) estimated a lateral DIC flux of 2.0 g C m^{-2} d^{-1} during winter and 3.0 g C m^{-2} d^{-1} during summer months (Chu et al. 2018), comparable to the $^{224}Ra : ^{228}Th$ DIC fluxes estimated here.

The DIC flux method comparison demonstrates that the $^{224}Ra : ^{228}Th$ disequilibria method effectively captures DIC export to the tidal creek. The $^{224}Ra : ^{228}Th$ disequilibria method should best represent marsh pore water exchange and DIC export in the absence of high-resolution time-series monitoring, or under conditions in which CO_2 is rapidly degassed to the atmosphere upon discharge (Raymond et al. 2000). Low marsh CO_2 evasion varies seasonally with temperature and substrate availability (Morris and Whiting 1986). At Sage Lot Pond, summertime low marsh CO_2 uptake exceeds emissions (Moseman-Valtierra et al. 2016), although annual CO_2 fluxes are unknown. In North Inlet, the annual CO_2 flux is estimated between 220 and 330 g C m^{-2} y^{-1} (Morris and Whiting 1986). If the magnitude of this net annual CO_2 emission is comparable to Sage Lot Pond, then CO_2 loss could potentially explain the differences in annual DIC exports between the tidal creek models and $^{224}Ra : ^{228}Th$-based approaches, in addition to inter-annual flux variability.

Finally, results confirm that salt marsh DIC export at Sage Lot Pond is exceptionally higher than previously estimated fluxes for other study areas including Duplin River, Georgia (156 g C m^{-2} y^{-1}; Wang and Cai 2004), North Inlet, South Carolina (175 g C m^{-2} y^{-1}; Morris and Whiting 1986) and San Francisco Bay Estuary (96 g C m^{-2} y^{-1}; Bogard et al. 2020).

This discrepancy between Sage Lot Pond and other study locations is likely due to differences in measurement techniques and considered time-scales (Wang et al. 2016; Chu et al. 2018), with the exception of San Francisco Bay. Alternatively, microtidal settings may sustain a disproportionate flux of DIC compared to macrotidal settings.

Carbon budget

The annual average marsh-derived DIC flux to Sage Lot Pond was previously estimated as 414 g C m^{-2} y^{-1} from 2012 to 2014 (Wang et al. 2016), or approximately four times the annual rate of organic carbon burial (120 ± 50 g C m^{-2} y^{-1}; Gonneea et al. 2019). This export is ultimately supported by high rates of CO_2 uptake by tidal wetland plants. At Sage Lot Pond, peak annual standing stock plant biomass in the low marsh, including stems, leaves, roots, and shoots, has been previously estimated as 2554 g C m^{-2} (calculated from Moseman-Valtierra et al. 2016). In a synthesis of literature on U.S. tidal wetland carbon budgets, Najjar et al. (2018) estimated that ~ 65% of annual CO_2 uptake by tidal wetland plants as Net Primary Production is respired by heterotrophs and returned to the atmosphere as "degassed" CO_2, while ~ 80% of the residual, equivalent to Net Ecosystem Exchange, is exported as a lateral flux. Based on those proportions, at Sage Lot Pond annual production could yield 1660 g C m^{-2} y^{-1} of degassing of heterotrophic respiration, 715 g C m^{-2} y^{-1} of total lateral flux, and 179 g C m^{-2} y^{-1} of net soil carbon storage, indicating that there is adequate fixed and respired carbon to support rates of pore water DIC export similar to those measured in the present study. There are a number of considerations that may result in yet greater measured DIC flux than calculated in this annual budget. First, some portion of autotrophic respiration, not represented in the annual budget calculated here, is likely to be conveyed by pore water exchange. Yet, an unknown portion of the autotrophic and heterotrophic respiration carried by pore water exchange is likely to rapidly return to the atmosphere as a degassing flux

following discharge. That degassing would then be captured in Net Ecosystem Exchange measurements by the eddy covariance technique (e.g., Forbrich et al. 2018). Secondly, allochthonous carbon, supplied by deposition of estuarine sediment and algal and detrital organic matter (e.g., Tobias and Neubauer 2009; Tzortziou et al. 2011), likely contributes to respired C fluxes. Finally, the temporal variability in DIC flux rates observed in the present study suggests that steady-state budgets are unlikely to occur in any given year.

Temporal variability

Periods of higher mean sea level (spring and summer 2019) coincide with periods of elevated marsh pore water exchange (Fig. 10). Conceptually, lower mean sea levels should result in (1) a smaller area of the marsh drainage basin inundated by seawater at high tide and (2) less frequent tidal inundation. This hypothesis is supported by the tidal time series and is independently observed from the interfacial ^{224}Ra fluxes (Fig. 5). Thus, periods of relatively high sea level should facilitate an increase in both deep, lateral DIC export and interfacial DIC export. This may be extended to other solutes enriched in shallow marsh sediments (e.g., NH_4^+, Mn, Fe) that impact carbon and nutrient "outwelling" and thus coastal productivity (Teal 1962; Odum 1968; Krest et al. 2000).

It remains to be seen how lower mean sea levels would impact soil saturation and thus storativity at Sage Lot Pond. The unsaturated zone of the marsh platform is very shallow (typically < 5 cm). If marsh platforms are recharged by seawater less frequently (vertical infiltration at high tide and at depth via the tidal creek), then less water would be available for exchange and DIC export. Wilson et al. (2015) observed a linear relationship between marsh groundwater discharge, mean water level and tidal amplitude, demonstrating that discharge decreases as sea-level increases. Guimond et al. (2020b) found a similar relationship between sea-level rise and lateral water fluxes, and further demonstrated that reduction in lateral water flux is minimized when the terrestrial groundwater table rises in concert with sea level. In both of these cases (respectively, Cabretta Island, Georgia and Dover, Delaware), rising sea levels reduce the hydraulic gradient between the water table and the coastal ocean. Differences between these systems with Sage Lot Pond may be related to differences in water table depth and tidal oscillation, and thus differences in sediment composition. Hydraulic head at Sage Lot Pond (site 1 mid station) is temporally variable but does not appear to be influenced by tides, and does not show any trend with tidal water elevation or amplitude (Supporting Information; Fig. S2).

At Sage Lot Pond, between 10% and 15% of the tides disproportionally skew the monthly mean DIC flux towards greater exports, some of which may be linked to episodic events (Chu et al. 2018). Sediment ^{224}Ra : ^{228}Th activity ratios approach secular equilibrium at depth within the marsh interior, such that pore water residence times are relatively longer

where pore water DIC concentrations are highest. Flushing of the marsh interior sediment during or after an extreme event may supply a disproportionate amount of DIC compared to near creekbank sediments. Wilson et al. (2011) observed a 50% reduction in marsh groundwater discharge in response to the passage of a distant tropical storm. Marsh site 2 (mid station) was sampled a day after a moderate storm event (35.4 mm precipitation, 23 July 2019). Marsh pore water exchange for this core was half that of site 1, while drainage was comparable between sites during winter 2018. Interestingly, pore water DIC concentrations at this station after the storm event (9.0 mM; salinity 33) were two-fold less than the creek station sampled just a few days prior (17.8 mM), suggesting that the interior marsh sediment was rapidly flushed by seawater. Lateral DIC flux during this period increases from 2.5 to 5.6 g C m^{-2} d^{-1} when using the creek station DIC end-member (i.e., ^{224}Ra : ^{228}Th integrates over 10 d while DIC does not). More work is ultimately required to understand the spatiotemporal variability of marsh pore water exchange and DIC flux in response to extreme events.

Spatial variability

Seasonal measurements of ^{224}Ra : ^{228}Th disequilibria in tidal marsh sediments were used to constrain the key spatial positions of marsh pore water exchange and associated DIC export. This approach integrates subsurface pathways over a ~ 10-day period and is thus ideal to determine DIC export averaged over multiple tidal cycles. Shallow sediment sections indicate that low marsh elevation zones nearest to the tidal creek are flushed more frequently than high marsh elevation zones, driven by tidal overtopping. This shallow depth zone (~ 0–5 cm) supplies an interfacial DIC flux from 0.0 to 0.7 g C m^{-2} d^{-1} that may increase in magnitude with increasing sea levels. However, the majority of the marsh DIC flux (1.7–5.4 g C m^{-2} d^{-1}) is derived from low marsh sediment horizons intersected by mean low tide, driven by tidal pumping. Notably, similar coastal wetlands are likely to have similar spatial patterns in pore water exchange and DIC export.

Ra transport was not observed at the peat–sand interface, for any core. Numerical models predict the highest rates of advection to occur at the interface of lower conductivity peat deposits and higher conductivity sands (Wilson and Gardner 2006; Wilson and Morris 2012; Xiao et al. 2019). Rather, subsurface sediment profile ^{224}Ra : ^{228}Th activity ratio deficits, observed between -20 and -45-cm elevation for both summer and fall sampling periods, correspond to the equivalent elevation of mean low tide (neap–spring). This is also the elevation range over which creek water ^{224}Ra activities are highest (Fig. 8A). Below the mean low tide elevation, ^{224}Ra : ^{228}Th activity ratio deficits may be influenced by heterogeneity in macropore structures and buried rhizomes (e.g., fall 2019 mid core, -110 cm elevation; Fig. 4) and infauna burrowing within the tidal creek banks (e.g., summer 2019 creek core, -60 to -90 cm elevation; Fig. 3), a process

which may seasonally increase the effective permeability of the marsh sediment (Guimond et al. 2020a).

It is unclear why pore water DIC concentrations would differ between sites 1 and 2 when marsh pore water exchange is comparable. Pore water DIC concentrations should be controlled by microbial activity, the delivery of oxidants and subsurface residence time (Tamborski et al. 2017). Marsh site 2 is lower in the tidal frame and has a greater proportion of panne/pools compared to site 1; it remains to be seen how differences in elevation and geomorphology would impact DIC concentrations and flux. Differences may also arise due to variations in peat thickness (site 1 = 150 cm vs site 2 = 70 cm) and upland hydrology. At site 1, mid- and bottom-depth enrichments of sediment ^{224}Ra and ^{228}Th (Fig. 3) are supported by the long-term flow of brackish groundwater, where the decay of dissolved ^{228}Ra creates local enrichments of scavenged ^{228}Th. Sediment ^{224}Ra and ^{228}Th activities were relatively constant with depth at marsh site 2, signifying the absence of brackish groundwater transport.

Conclusions

This study focused on two different marsh hydrologic units within Sage Lot Pond, a microtidal estuary of the Northeast United States. A relatively new method, ^{224}Ra : ^{228}Th disequilibria in tidal marsh sediments, was used to constrain the key spatial positions of marsh pore water exchange and associated DIC export. Estimated DIC fluxes are in relative agreement with tidal creek-based modeling approaches. Importantly, the ^{224}Ra : ^{228}Th disequilibria approach demonstrates that the majority of lateral DIC exports are derived from low marsh sediment horizons intersected by mean low tide, driven by tidal pumping. Results suggest that area-normalized DIC flux can vary by a factor of four between two drainage basins within the same estuary. In addition to known seasonal variability, marsh pore water exchange and DIC flux likely vary annually, in part due to annual variations in sea-level. Continued sea-level rise may lead to greater lateral C exports. Together, this calls into question what the "true" magnitude of lateral DIC fluxes are at regional- and global-scales. In conclusion, lateral DIC export is a major carbon flux term that requires further study across tidal, environmental (sediment type, elevation, vegetation) and latitudinal gradients.

References

Bauer, J. E., W.-J. Cai, P. A. Raymond, T. S. Bianchi, C. S. Hopkinson, and P. A. G. Regnier. 2013. The changing carbon cycle of the coastal ocean. Nature **504**: 61–70. doi:10.1038/nature12857

Bogard, M. J., B. Bergamaschi, D. Butman, F. Anderson, S. Knox, and L. Windham-Myers. 2020. Hydrologic export is a major component of coastal wetland carbon budgets. Global Biogeochem. Cycles **34**(8) e2019GB006430. doi:10.1029/2019GB006430

Bollinger, M. S., and W. S. Moore. 1993. Evaluation of salt marsh hydrology using radium as a tracer. Geochim. Cosmochim. Acta **57**: 2203–2212. doi:10.1016/0016-7037(93)90562-B

Brooks, T. W., M. Eagle, K. D. Kroeger, A. G. Mann, Z. A. Wang, N. K. Ganju, J. A. O'Keefe Suttles, S. B. Brosnahan, Chu, S. N., Song, S., Pohlman, J. W., Casso, M., Tamborski, J. J., Morkeski, K., Carey, J. C., Ganguli, P. M., Williams, O. L., and Kurtz, A. C. 2021. Geochemical data supporting investigation of solute and particle cycling and fluxes from two tidal wetlands on the south shore of Cape Cod, Massachusetts, Geological Survey data release, U.S. 2012-19. doi:10.5066/P9MXLUZ1

Cai, P., X. Shi, W. S. Moore, and M. Dai. 2012. Measurement of ^{224}Ra:^{228}Th disequilibrium in coastal sediments using a delayed coincidence counter. Mar. Chem. **138–139**: 1–6. doi:10.1016/j.marchem.2012.05.004

Cai, P., X. Shi, W. S. Moore, S. Peng, G. Wang, and M. Dai. 2014. ^{224}Ra:^{228}Th disequilibrium in coastal sediments: Implications for solute transfer across the sediment-water interface. Geochim. Cosmochim. Acta **125**: 68–84. doi:10.1016/j.gca.2013.09.029

Cai, P., X. Shi, Q. Hong, Q. Li, L. Liu, X. Guo, and M. Dai. 2015. Using ^{224}Ra/^{228}Th disequilibrium to quantify benthic fluxes of dissolved inorganic carbon and nutrients into the Pearl River estuary. Geochim. Cosmochim. Acta **170**: 188–203. doi:10.1016/j.gca.2015.08.015

Cai, W.-J. 2011. Estuarine and Coastal Ocean carbon paradox: CO_2 sinks or sites of terrestrial carbon incineration? Ann. Rev. Mar. Sci. **3**: 123–145. doi:10.1146/annurev-marine-120709-142723

Charette, M. A. 2007. Hydrologic forcing of submarine groundwater discharge: Insight from a seasonal study of radium isotopes in a groundwater-dominated salt marsh estuary. Limnol. Oceanogr. **52**: 230–239. doi:10.4319/lo.2007.52.1.0230

Chu, S. N., Z. A. Wang, M. E. Gonneea, K. D. Kroeger, and N. K. Ganju. 2018. Deciphering the dynamics of inorganic carbon export from intertidal salt marshes using high-frequency measurements. Mar. Chem. **206**: 7–18. doi:10.1016/J.MARCHEM.2018.08.005

Dickson, A. G., G. Andrew, C. L. Sabine, J. R. Christian, and North Pacific Marine Science Organization. 2007. Guide to best practices for ocean CO_2 measurements. North Pacific Marine Science Organization.

Forbrich, I., A. E. Giblin, and C. S. Hopkinson. 2018. Constraining marsh carbon budgets using long-term C burial and contemporary atmospheric CO_2 fluxes. J. Geophys. Res. Biogeo. **123**: 867–878. doi:10.1002/2017JG004336

Gonneea, M. E., and others. 2019. Salt marsh ecosystem restructuring enhances elevation resilience and carbon storage during accelerating relative sea-level rise. Estuar. Coast. Shelf Sci. **217**: 56–68. doi:10.1016/J.ECSS.2018.11.003

Guimond, J., A. L. Seyfferth, K. Moffett, and H. Michael. 2020*a*. A physical-biogeochemical mechanism for negative feedback between marsh crabs and carbon storage. Environ. Res. Lett. **15**: 034024. doi:10.1088/1748-9326/ab60e2

Guimond, J. A., X. Yu, A. L. Seyfferth, and H. A. Michael. 2020*b*. Using hydrological-biogeochemical linkages to elucidate carbon dynamics in coastal marshes subject to relative sea-level rise. Water Resour. Res. **56**: e2019WR026302. doi:10.1029/2019WR026302

Harvey, J. W., P. F. Germann, and W. E. Odum. 1987. Geomorphological control of subsurface hydrology in the creekbank zone of tidal marshes. Estuar. Coast. Shelf Sci. **25**: 677–691. doi:10.1016/0272-7714(87)90015-1

Harvey, J. W., and W. E. Odum. 1990. The influence of tidal marshes on upland groundwater discharge to estuaries. Biogeochemistry **10**: 217–236.

Harvey, J. W., and W. K. Nuttle. 1995. Fluxes of water and solute in a coastal wetland sediment. 2. Effect of macropores on solute exchange with surface water. J. Hydrol. **164**: 109–125.

Herrmann, M., and others. 2015. Net ecosystem production and organic carbon balance of U.S. East Coast estuaries: A synthesis approach. Global Biogeochem. Cycles **29**: 96–111. doi:10.1002/2013GB004736

Krest, J. M., W. S. Moore, L. R. Gardner, and J. T. Morris. 2000. Marsh nutrient export supplied by groundwater discharge: Evidence from radium measurements. Global Biogeochem. Cycles **14**: 167–176.

Mann, A. G., J. A. O'Keefe Suttles, M. E. Gonneea, S. M. Brosnahan, T. W. Brooks, Z. A. Wang, N. K. Ganju, and K. D. Kroeger. 2019. Time-series of biogeochemical and flow data from a tidal salt-marsh creek, sage lot pond, Waquoit Bay, Massachusetts (2012-2016): U.S. Geological Survey Data Release. https://doi.org/10.5066/P9STIROQ

Mcleod, E., and others. 2011. A blueprint for blue carbon: Toward an improved understanding of the role of vegetated coastal habitats in sequestering CO_2. Front. Ecol. Environ. **9**: 552–560. doi:10.1890/110004

Moffett, K. B., S. M. Gorelick, R. G. McLaren, and E. A. Sudicky. 2012. Salt marsh ecohydrological zonation due to heterogeneous vegetation-groundwater-surface water interactions. Water Resour. Res. **48**: 22. doi:10.1029/2011WR010874

Moore, W. S. 2003. Sources and fluxes of submarine groundwater discharge delineated by radium isotopes. Biogeochemistry **66**: 75–93. doi:10.1023/B:BIOG.0000006065.77764.a0

Moore, W. S., and R. Arnold. 1996. Measurement of Ra-223 and Ra-224 in coastal waters using a delayed coincidence counter. J. Geophys. Res. Oceans **101**: 1321–1329. doi:10.1029/95JC03139

Morris, J. T., and G. J. Whiting. 1986. Emission of gaseous carbon dioxide from salt-marsh sediments and its relation to other carbon losses. Estuaries **9**: 9–19. doi:10.2307/1352188

Morris, J. T., and others. 2016. Contributions of organic and inorganic matter to sediment volume and accretion in tidal wetlands at steady state. Earth's Future **4**: 110–121. doi:10.1002/2015EF000334

Moseman-Valtierra, S., O. I. Abdul-Aziz, J. Tang, and others. 2016. Carbon dioxide fluxes reflect plant zonation and belowground biomass in a coastal marsh. Ecosphere **7**: e01560. doi:10.1002/ecs2.1560

Najjar, R. G., and others. 2018. Carbon budget of tidal wetlands, estuaries, and shelf waters of eastern North America. Global Biogeochem. Cycles **32**: 389–416. doi:10.1002/2017GB005790

Neubauer, S. C., and I. C. Anderson. 2003. Transport of dissolved inorganic carbon from a tidal freshwater marsh to the York River estuary. Limnol. Oceanogr. **48**: 299–307. doi:10.4319/lo.2003.48.1.0299

Nuttle, W. K., and H. F. Hemmond. 1988. Salt marsh hydrology: Implications for biogeochemical fluxes to the atmosphere and estuaries. Global Biogeochem. Cycles **2**: 91–114.

OCM Partners. 2020. 2011 U.S. Geological Survey Topographic LiDAR: LiDAR for the north east.

Odum, E. P. 1968. Energy flow in ecosystems: A historical review. Integrative and Comparative Biology **8**: 11–18. doi:10.1093/icb/8.1.11

Rama, and W. S. Moore. 1996. Using the radium quartet for evaluating groundwater input and water exchange in salt marshes. Geochim. Cosmochim. Acta **60**: 4645–4652. doi:10.1016/S0016-7037(96)00289-X

Raymond, P. A., J. E. Bauer, and J. J. Cole. 2000. Atmospheric CO_2 evasion, dissolved inorganic carbon production, and net heterotrophy in the York River estuary. Limnol. Oceanogr. **45**: 1707–1717. doi:10.4319/lo.2000.45.8.1707

Santos, I. R., D. T. Maher, R. Larkin, J. R. Webb, and C. J. Sanders. 2019. Carbon outwelling and outgassing vs. burial in an estuarine tidal creek surrounded by mangrove and saltmarsh wetlands. Limnol. Oceanogr. **64**: 996–1013. doi:10.1002/lno.11090

Shi, X., C. R. Benitez-Nelson, P. Cai, L. He, and W. S. Moore. 2019. Development of a two-layer transport model in layered muddy-permeable marsh sediments using ^{224}Ra-^{228}Th disequilibria. Limnol. Oceanogr. **64**: 1672–1687. doi:10.1002/lno.11143

Tamborski, J. 2020. Sage lot pond Ra isotope data 2018-2019. HydroShare. doi:https://doi.org/10.4211/hs.f73a4683b3f45d5a4cb523578ab639d

Tamborski, J. J., J. K. Cochran, C. Heilbrun, P. Rafferty, P. Fitzgerald, Q. Zhu, and C. Salazar. 2017. Investigation of pore water residence times and drainage velocities in salt marshes using short-lived radium isotopes. Mar. Chem. **196**: 107–115. doi:10.1016/j.marchem.2017.08.007

Taniguchi, M., H. Dulai, K. M. Burnett, I. R. Santos, R. Sugimoto, T. Stieglitz, G. Kim, N. Moosdorf, and W. C. Burnett. 2019. Submarine groundwater discharge: Updates on its measurement techniques, geophysical drivers, magnitudes, and effects. Front. Environ. Sci. **7**: 1–26. doi:10.3389/fenvs.2019.00141

Teal, J. M. 1962. Energy flow in the salt marsh ecosystem of Georgia. Ecology **43**: 614–624. doi:10.2307/1933451

Tobias, C., and S. C. Neubauer. 2009. Salt marsh biogeochemistry: An overview, p. 445–492.*In* Coastal wetlands: An integrated ecosystem approach. Elsevier Science. doi:10.1016/B978-0-444-63893-9.00016-2

Tzortziou, M., P. J. Neale, P. Megonigal, C. L. Pow, and M. Butterworth. 2011. Spatial gradients in dissolved carbon due to tidal marsh outwelling into a Chesapeake Bay estuary. Mar. Ecol. Prog. Ser. **426**: 41–56. doi:10.3354/meps09017

Wang, Z. A., and W.-J. Cai. 2004. Carbon dioxide degassing and inorganic carbon export from a marsh-dominated estuary (the Duplin River): A marsh CO_2 pump. Limnol. Oceanogr. **49**: 341–354. doi:10.4319/lo.2004.49.2.0341

Wang, Z. A., K. D. Kroeger, N. K. Ganju, M. E. Gonneea, and S. N. Chu. 2016. Intertidal salt marshes as an important source of inorganic carbon to the coastal ocean. Limnol. Oceanogr. **61**: 1916–1931. doi:10.1002/lno.10347

Wasson, K., K. Raposa, M. Almeida, and others. 2019. Pattern and scale: Evaluating generalities in crab distributions and marsh dynamics from small plots to a national scale. Ecology **100**: e02813. doi:10.1002/ecy.2813

Wilson, A. M., and L. R. Gardner. 2006. Tidally driven groundwater flow and solute exchange in a marsh: Numerical simulations. Water Resour. Res. **42**: W01405. doi:10.1029/2005WR004302

Wilson, A. M., W. S. Moore, S. B. Joye, J. L. Anderson, and C. A. Schutte. 2011. Storm-driven groundwater flow in a salt marsh. Water Resour. Res. **47**: W02535. doi:10.1029/2010WR009496

Wilson, A. M., and J. T. Morris. 2012. The influence of tidal forcing on groundwater flow and nutrient exchange in a salt marsh-dominated estuary. Biogeochemistry **108**: 27–38. doi:10.1007/s10533-010-9570-y

Wilson, A. M., T. Evans, W. Moore, C. A. Schutte, and S. B. Joye. 2015. What time scales are important for monitoring tidally-influenced submarine groundwater discharge? Insights from a salt marsh. Water Resour. Res. **51**: 4198–4207. doi:10.1002/2014WR015984

Xiao, K., A. M. Wilson, H. Li, and C. Ryan. 2019. Crab burrows as preferential flow conduits for groundwater flow and transport in salt marshes: A modeling study. Adv. Water Resour. **103408**: 103408. doi:10.1016/J.ADVWATRES.2019.103408

Xin, P., L.-R. Yuan, L. Li, and D. A. Barry. 2011. Tidally driven multiscale pore water flow in a creek-marsh system. Water Resour. Res. **47**: W07534. doi:10.1029/2010WR010110

Xin, P., J. Kong, L. Li, and D. A. Barry. 2013. Modelling of groundwater-vegetation interactions in a tidal marsh. Adv. Water Resour. **57**: 52–68. doi:10.1016/j.advwatres.2013.04.005

Conflict of Interest

None declared.